

Method Dependence in Thermal Conductivity and Aerodynamic Roughness Length Estimates on a Debris-Covered Glacier


Key Points:

- We derive k and z_0 using established methods to estimate ice melt with an energy-balance (EB) model
- Different methods yield distinct results, and generally fail to match observed ablation when used in an EB model
- The discrepancies between measured and optimized k values for EB models suggest more work on debris conductivity is needed

Vicente Melo-Velasco¹ , Evan Miles^{2,3,4} , Michael McCarthy^{1,2,5} , Thomas E. Shaw¹ , Catriona Fyffe¹ , Adrià Fontrodona-Bach¹ , and Francesca Pellicciotti¹ 

¹Institute of Science and Technology Austria, ISTA, Klosterneuburg, Austria, ²Swiss Federal Institute for Forest, Snow and Landscape Research WSL, Birmensdorf, Switzerland, ³Department of Geography, University of Zurich, Glaciology and Geomorphodynamics Group, Zurich, Switzerland, ⁴Department of Geosciences, University of Fribourg, Fribourg, Switzerland, ⁵British Antarctic Survey, Natural Environment Research Council, Cambridge, UK

Supporting Information:

Supporting Information may be found in the online version of this article.

Correspondence to:

V. Melo-Velasco,
Vicente.MeloVelasco@ista.ac.at

Citation:

Melo-Velasco, V., Miles, E., McCarthy, M., Shaw, T. E., Fyffe, C., Fontrodona-Bach, A., & Pellicciotti, F. (2025). Method dependence in thermal conductivity and aerodynamic roughness length estimates on a debris-covered glacier. *Journal of Geophysical Research: Earth Surface*, 130, e2025JF008360. <https://doi.org/10.1029/2025JF008360>

Received 11 FEB 2025
Accepted 28 MAY 2025

Abstract Rock debris partially covers glaciers worldwide, with varying extents and distributions, and controls sub-debris melt rates by modifying energy transfer from the atmosphere to the ice. Two key physical properties controlling this energy exchange are thermal conductivity (k) and aerodynamic roughness length (z_0). Accurate representation of these properties in energy-balance models is critical for understanding climate-glacier interactions and predicting the behavior of debris-covered glaciers. However, k and z_0 have been derived at very few sites from limited local measurements, using different approaches, and most model applications rely on values reported from these few sites and studies. We derive k and z_0 using established and modified approaches from data at three locations on Pirámide Glacier in the central Chilean Andes. By comparing methods and evaluating melt simulated with an energy-balance model, we reveal substantial differences between approaches. These lead to discrepancies between ice melt from energy-balance simulations and observed data, and highlight the impact of method choice on calculated ice melt. Optimizing k against measured melt appears a viable approach to constrain melt simulations. Determining z_0 seems less critical, as it has a smaller impact on total melt. Profile aerodynamic method measurements for estimating z_0 , despite higher costs, are independent of ice melt calculations. The large, unexpected differences between methods indicate a substantial knowledge gap. The fact that field-derived k and z_0 fail to work well in energy-balance models, suggests that model values represent bulk properties distinct from theoretical field measurements. Addressing this gap is essential for improving glacier melt predictions.

Plain Language Summary Debris on glaciers affects how quickly the ice underneath melts by controlling how heat moves from the air to the ice. Key properties like thermal conductivity (k) and aerodynamic roughness length (z_0) are rarely measured directly and are often taken from other studies. Representing these properties accurately in energy-balance models is important for understanding how glaciers interact with the climate. In our study on Pirámide Glacier (Chile), we compare and evaluate how accurately we can model sub-debris melt when using values of k and z_0 derived from existing methods. We found that methods for calculating k and z_0 can give very different results, and most lead to mismatches between modeled and observed ice melt. Optimizing k using measured ice melt and temperature data works well for energy-balance modeling. While determining z_0 is less critical, the profile aerodynamic method-derived estimates are preferable since they do not rely on the energy-balance model itself. The differences between methods reveal a significant knowledge gap. Overall, values of k and z_0 from field measurements often do not match what energy-balance models need to reproduce melt, showing that field-based and model-based values do not align, highlighting the need for more research to close the gap.

1. Introduction

Rocky debris partially covers 44% of Earth's glaciers (excluding Antarctica) and is prominent (over 1.0 km²) on 15% of them (Herreid & Pellicciotti, 2020). These glaciers are common in many mountain ranges, including High-Mountain Asia, the European Alps, the Andes, the Alaska Range and New Zealand's Southern Alps (Herreid & Pellicciotti, 2020). Supraglacial debris influences ablation patterns and leads to distinct glacier evolution (Anderson & Anderson, 2016; Compagno et al., 2022; Gibson et al., 2017; Nicholson & Benn, 2006; Reid et al., 2012; Rounce et al., 2021; Rowan et al., 2015). Understanding how these glaciers evolve is critical as

© 2025. The Author(s).

This is an open access article under the terms of the [Creative Commons Attribution License](https://creativecommons.org/licenses/by/4.0/), which permits use, distribution and reproduction in any medium, provided the original work is properly cited.

debris-covered glaciers are projected to increase with climate warming (Anderson & Anderson, 2018; Fischer et al., 2013; Gruber & Haeberli, 2007).

Debris thickness is a key factor influencing melt rates and it can vary from fine dust to layers several meters thick (McCarthy et al., 2017; Nicholson et al., 2018), influenced by gravitational reworking (Moore, 2018), englacial debris melt-out (Swithinbank, 1950) and ice flow displacement (Anderson & Anderson, 2018; Fyffe et al., 2020; Westoby et al., 2020). We understand from numerical modeling and field data the overall relationship between debris thickness and ablation rates: thin debris layers (less than a few centimeters) enhance melt, while thicker debris reduces it (Nicholson & Benn, 2006; Reid & Brock, 2010; Östrem, 1959). However, key properties of the debris layer, such as thermal conductivity (Evatt et al., 2015; Fyffe et al., 2014; Rounce et al., 2015), albedo (Fujita & Sakai, 2014), porosity (Juen et al., 2013), aerodynamic roughness length (Miles et al., 2017; Rounce et al., 2015) and moisture content (Giese et al., 2020; Steiner et al., 2021), modulate this relationship and influence how efficiently energy is transferred from the atmosphere to the ice through the debris layer. Thermal conductivity (k), aerodynamic roughness length ($z_{0,M}$, hereafter z_0) and albedo (α) have all been shown to be important in modeling ice melt (Fyffe et al., 2014; Rounce et al., 2015; Steiner et al., 2021). However, while α is relatively easy to measure and commonly documented, thermal conductivity and aerodynamic roughness length are challenging to measure directly and therefore rarely reported. k in particular has been identified as a particularly sensitive factor in sub-debris melt estimates (Fyffe et al., 2014; Miles et al., 2022; Rounce et al., 2015; Steiner et al., 2021). The sensitivity to z_0 is more debated: Rounce et al. (2015) found ablation rates to be most sensitive to k , followed closely by z_0 and α , while Fyffe et al. (2014) reported that, at the glacier scale, simulated melt rates are largely unaffected by changes in z_0 within the range tested.

Given that the measurements required to derive k and z_0 are rarely made, many modeling studies rely on previously published values. Importantly, even when these measurements are collected, multiple methods exist for deriving these properties, each with different assumptions, strengths and limitations. These methods have not, with some exceptions, been systematically compared to evaluate their impact on sub-debris melt. This study addresses these gaps by conducting an observational campaign at Pirámide Glacier in Chile to investigate the thermal conductivity and aerodynamic roughness length of supraglacial debris to answer the following research questions:

1. How do the estimates of thermal conductivity and aerodynamic roughness length from the most commonly used methods based on field measurements compare to each other?
2. When used in an energy-balance model, are the calculated values of thermal conductivity and aerodynamic roughness length able to simulate melt consistent with ablation measurements?

To address these questions, we used established approaches, and variations on those approaches, to derive k and z_0 from field measurements. We then conducted point-scale energy-balance modeling using the k and z_0 values obtained to evaluate how differences propagate into the simulated melt rates and how well the latter compare to measured ice melt.

Deriving debris thermal conductivity from field measurements was first attempted by Nakawo and Young (1982). Their method assumes that the temperature profile of the debris layer is constant, with no heat conducted into the ice, and requires measurements of debris thickness, surface temperature and ablation. Brock et al. (2010) applied this method but also measured the temperature at the ice-debris interface, assuming a linear mean vertical gradient and negligible net heat change in debris over time, an assumption valid for periods exceeding a week (Conway & Rasmussen, 2000; Nicholson & Benn, 2012). Conway and Rasmussen (2000) calculated thermal diffusivity (κ) using vertical temperature profiles and the one-dimensional diffusion equation, assuming purely conductive conditions. This method requires knowledge of the debris layer's lithology, porosity and moisture content to compute k (Nicholson & Benn, 2012; Steiner et al., 2021). Laha et al. (2022) adapted this approach to account for inhomogeneities in debris thermal properties using a two-layered model. Fugger et al. (2022) optimized k against ablation and surface temperature measurements by simulating energy conduction through a homogeneous debris cover during snow-free periods.

The profile aerodynamic method has been used to derive the aerodynamic roughness length of debris surfaces based on Monin-Obukhov similarity theory (e.g., Chambers et al., 2020; Miles et al., 2017; Quincey et al., 2017; Sicart et al., 2014). Under idealized surface boundary layer conditions (horizontal, homogeneous and steady-state), the turbulent characteristics of the surface boundary layer can be described using turbulent velocity and

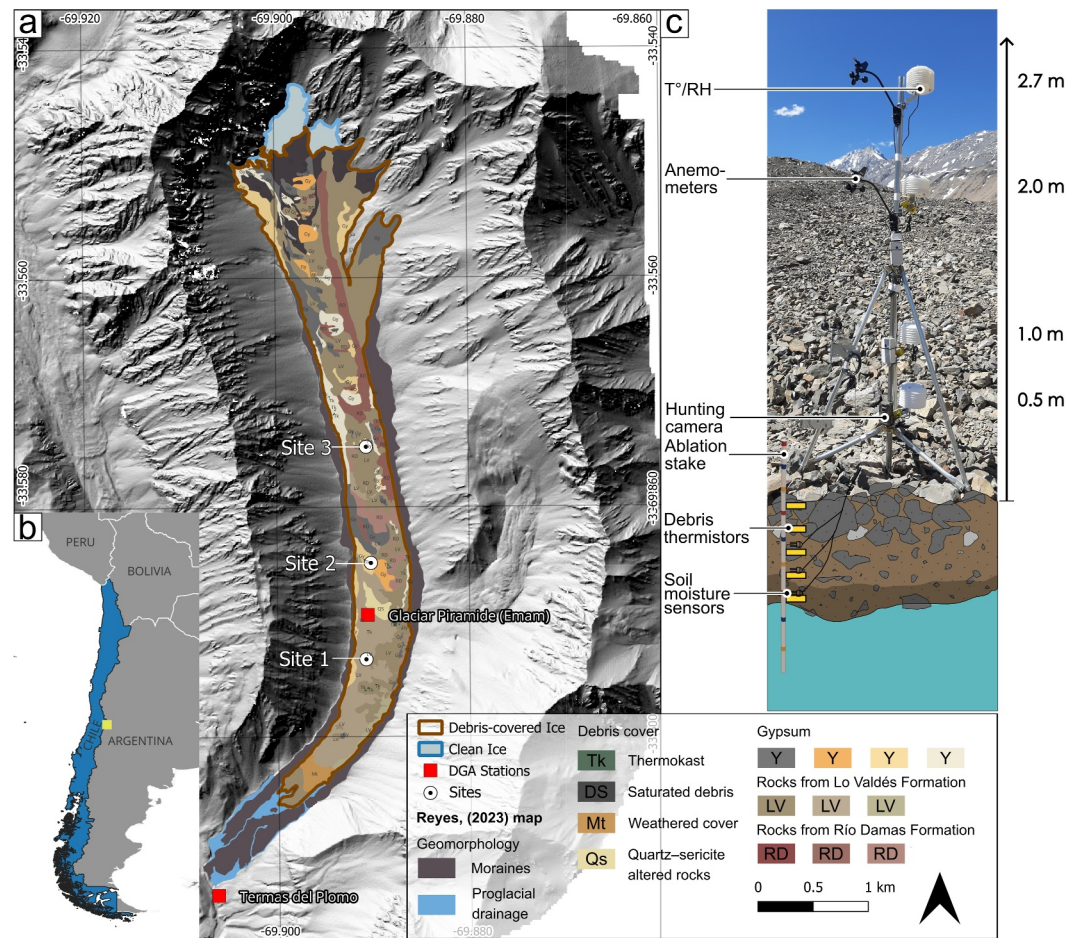


Figure 1. (a) Map of Pirámide Glacier showing debris cover extent, locations of the study sites (AWSs, debris thermistors, soil moisture and ablation stakes) and the long-term AWSs operated by the DGA. The lithological map highlights changes in debris cover type (even within a single lithology or Formation) (modified by Reyes Kutscher, 2023, with permission from the author), underlain by a 2018 Pleiades-derived DEM hillshade (Shaw et al., 2020). (b) Location of Pirámide Glacier in the Andes of Central Chile (yellow square). (c) Diagram of the experimental setup at site 1, including the AWS and in-debris sensors (location of the ablation stake and in-debris sensors not to scale).

temperature scales, along with length scales and aerodynamic roughness lengths for momentum and temperature. Alternatively, optimization approaches for energy-balance modeling (e.g., Fugger et al., 2022; Steiner et al., 2021) have calibrated z_0 to reproduce observed ice melt, mass loss or surface temperature. z_0 has also been derived from microtopographic methods using: (a) Mechanistic approaches (Lettau, 1969; Munro, 1989), which use elevation profiles to identify obstacles; and (b) empirical approaches, which use detrended DEMs of equal height and width to calculate the standard deviation of elevations and estimate z_0 from empirical parameterizations (Nield, Chiverrell, et al., 2013; Nield, King, et al., 2013). Finally, turbulent fluxes measured using an eddy covariance system can be used to calculate z_0 at the point scale (Nicholson & Stiperski, 2020; Steiner et al., 2018).

2. Study Site, Data and Methods

2.1. Study Site

Our study focuses on the debris-covered Pirámide Glacier in the Rio Yeso catchment, Central Chile, about 70 km east of Santiago (Figures 1a and 1b). The catchment is 19% glacierized (Ayala et al., 2016; Burger et al., 2018) and located in the semiarid Andes, characterized by cold, humid winters and hot, dry summers (Ayala et al., 2016; Schaefer et al., 2020). Precipitation is mainly during winter and highly variable (Falvey & Garreaud, 2009), and the region has experienced a prolonged megadrought since 2010 (Boisier et al., 2016; Garreaud et al., 2020, 2021).

Pirámide Glacier ranges from 3,200 to 4,600 m a.s.l., averaging 3,670 m a.s.l., covering 4.4 km² over 7.5 km and is almost entirely debris-covered (Ayala et al., 2016; Schaefer et al., 2020). It lacks a defined accumulation area, gaining mass primarily from avalanches off steep headwall slopes (Burger et al., 2018). The glacier is nearly stagnant, with annual velocities <5 m a⁻¹ (Millan et al., 2022) and has had minimal area loss compared to other regional glaciers (Janke et al., 2015). Its mass balance shows no significant variation with altitude, controlled by debris cover and avalanches (Ayala et al., 2016).

The debris on Pirámide Glacier is composed mainly of rocks from the Lo Valdés and Río Damas Formations and gypsum. The Lo Valdés Formation consists of intercalated marine sedimentary and volcanic rocks, while the Río Damas Formation is mainly sandstones (Reyes Kutscher, 2023). These lithologies have distinct properties, such as specific heat capacity and density (Waples & Waples, 2004), affecting the thermal properties of the debris layer.

2.2. Data

2.2.1. Meteorological Measurements

Three automatic weather stations (towers) were installed on the glacier, equipped with air temperature, relative humidity and wind speed sensors at four heights (0.5, 1, 2 and 2.7 m) (Figure 1, Table 1). They operated from late November 2022 to early March 2023. Tower 1 remained upright throughout, while the other two toppled (see dates in Table 1).

Air temperature and relative humidity were measured using TinyTag Plus 2 (TG-4505) sensor–logger units, with accuracies of $\pm 0.35^{\circ}\text{C}$ and $\pm 3.0\%$ respectively. The sensors were shielded using an ACS-5050 Stevenson Screen. Wind speed and direction were measured using two different sensor types due to logger limitations, which allowed only one connection per sensor type. Davis Pro-D anemometers (accuracy: 0.89 m s^{-1}) were installed at 2 and 2.7 m heights to record both wind speed and direction, while Vortex anemometers (accuracy: 0.45 m s^{-1}) were used at 0.5 and 1 m heights to measure wind speed only. Temperature and humidity were recorded at 10-min intervals and averaged to 30-min intervals for analysis, while wind speed was recorded at 1-min intervals and averaged to 30-min values (Figures S1–S3 in Supporting Information S1).

Daily air temperature patterns were consistent across the three sites (Figures 2a–2c). Comparing only the period when all three sites were operational (before 12/02/2023), the average temperatures at sites 1 and 2 were approximately the same (~ 8.93 and 8.92°C , respectively), whereas site 3 recorded lower temperatures (7.3°C). While daily averages do not show substantial temperature differences between different heights, the average daily temperature cycle shows that during the day, a negative vertical gradient is observed, with higher sensors recording cooler temperatures than lower ones within each site (Figures 3c–3g and 3k). Daytime and nighttime averages also show a temperature gradient between sites: site 1 is the warmest and site 3 the coolest. During the day, the vertical temperature gradients are -0.07 , -0.20 , and $-0.14^{\circ}\text{C m}^{-1}$ for sites 1, 2, and 3, respectively. At night, the gradients reverse to 0.24 , 0.25 , and $0.42^{\circ}\text{C m}^{-1}$ for the same sites (Figure 3 and Figure S5a in Supporting Information S1).

Daily averages of wind speed indicate a clear height-dependent pattern at all three sites, with higher wind speeds recorded at the upper sensors and lower speeds at the bottom (Figures 2d–2f). Average wind speeds show consistent differences between sites: site 1 has values approximately 0.1 – 0.4 m s^{-1} higher than site 3 and 0.1 – 0.5 m s^{-1} lower than site 2. All three sites exhibit relatively uniform vertical gradients, with values of 0.58 , 0.49 , and $0.42\text{ m s}^{-1}/\text{m}$ for sites 1, 2, and 3, respectively (Figures 2d–2f and Figure S5b in Supporting Information S1). There are two predominant wind directions observed at each site: One occurring in the early morning and another in the afternoon to early evening. These wind directions are roughly opposed at each tower, and there appears an anti-clockwise rotation from site 1 to site 3 (Figures 2d–2f and Figure S4 in Supporting Information S1).

2.2.2. In-Debris Measurements

In flat areas adjacent to each tower (not too close to avoid shading, not too far to maintain representativeness, and not too close to ice cliffs to avoid potential backwasting; see Table 1 for distances), five thermistors and three moisture sensors were installed within the debris at regular depth intervals between the debris surface and

Table 1
Locations and Dates of the Wind and Temperature Measurements (Towers) and the Debris Thermistors and Moisture Content Sensors

Site	Latitude [°]	Longitude [°]	Elevation [m a.s.l.]	W_s, T_{air} and RH measurement period		T_{deb} measurement period		θ measurement period		Debris thickness [cm] (± 2 cm)	T_{deb} sensor depths [cm] (± 2 cm)	θ sensor depths [cm] (± 2 cm)	Distance of in-debris sensors to tower [m]
				Start date	End date	Start date	End date	Start date	End date				
1	-33.5933	-69.8908	3,406	22/11/22 (0.5 and 2 m)	02/03/23 (0.5 and 2 m)	21/11/22	02/03/23	21/11/22	02/03/23	50	0, 12.5, 25.0, 37.5, 50.0	30.0, 40.0, 50.0	~3
2	-33.5849	-69.8902	3,487	22/11/22 (1 and 2.7 m) ^a	21/02/23 (1 and 2.7 m)	23/11/22	12/02/23 ^b	21/11/22	02/03/23	45	0, 11.0, 22.0, 33.0, 44.0	19.0, 29.0, 39.0	~3
3	-33.5748	-69.8907	3,619	24/11/22	07/12/22 ^b	21/11/22	06/03/23	21/11/22	02/03/23	24	0, 6.0, 12.0, 18.0, 24.0	12.0, 17.5, 21.5	~7

Note. The position of the in-debris sensors was rounded to the nearest 5 mm. ^aThe battery of the wind sensor logger failed on that day. ^bDay that the tower toppled over, determined by the pictures of the hunting camera.

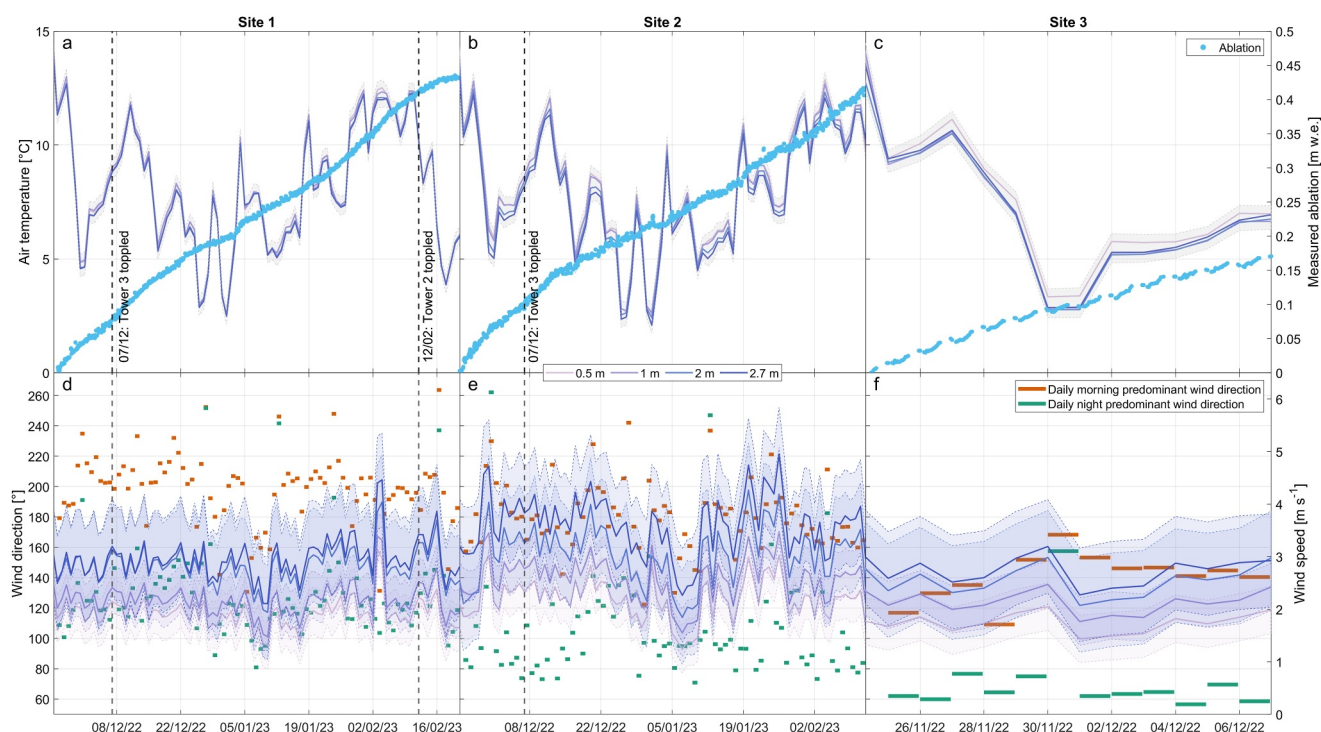


Figure 2. (a–c) Daily averages of air temperature and (d–f) wind speed at the different elevations, and (d–f) daytime/nighttime wind directions at the 2 m sensor. Shaded areas represent the sensor uncertainty (for air temperature a combined area is shown, since all the measurements are clustered at this scale). Vertical dashed lines indicate the times when the towers at sites 2 and 3 toppled. For the full data and distribution of wind directions see Text S1, Figures S1–S4 in Supporting Information S1). Ablation measurements from the hunting camera pictures are shown in blue. For sites 2 and 3 there is an additional measurement when the site was visited at the end of the period (see Figure 7).

the ice surface (Figures 1c, Table 1). Near-surface thermistors (labeled as 0 cm in Table 1) were covered with a thin debris layer (~2 cm), consisting of enough gravel-sized clasts to cover the sensor from direct radiation (Figure S6 in Supporting Information S1). Temperature was measured using Tinytag Transit 2 sensors (model TG-4080) with an accuracy of $\pm 0.4^{\circ}\text{C}$ and moisture content was measured using HOBO sensors (model S-SMC-M005) with an accuracy of $\pm 3\%$. Debris temperature measurements were taken at 30-min intervals and moisture content readings were recorded at 5-min intervals. At each site we recorded the observed lithologies, with which we calculated a weighted average rock density and specific heat capacity (Text S2 in Supporting Information S1).

Average temperature profiles within debris over the full measurement period are approximately linear, with linear regressions of sensor temperature versus depth yielding R^2 values ranging from 0.80 to 0.99 (Figures 3b–3f and 3j). The calculated temperature gradients range between 21.4 and $24.6^{\circ}\text{C m}^{-1}$. Diurnal debris temperature peak values at the surface range from -3 to 0°C at night and from 24 to 27°C during the day. Deeper sensors exhibit smoother daily cycles, with the timing of the temperature peak shifting later in the day and approaching a constant value of $\sim 0^{\circ}\text{C}$ at the base of the debris. The mean peak temperature transit time is similar for sites 1 and 2 (14.1 and 15.8 hr m^{-1}), while it is slightly shorter at site 3 (9.3 hr m^{-1}) (Figures 3c–3g and 3k).

2.2.3. Sub-Debris Ice Ablation

A 3 m PVC stake, marked at 10 cm intervals, was drilled into the ice at the pit excavated for the installation of the debris temperature and moisture sensors, ensuring that the debris thickness at the stake and thermistors was consistent. A Bushnell 24MP hunting camera captured hourly images of the ablation stake from 07:00 to 19:00, as well as one image at night (03:00). Tracker software, a free Java video analysis and modeling tool from Open Source Physics (<https://physlets.org/tracker/>), was used to read changes in length of exposed stake. For our

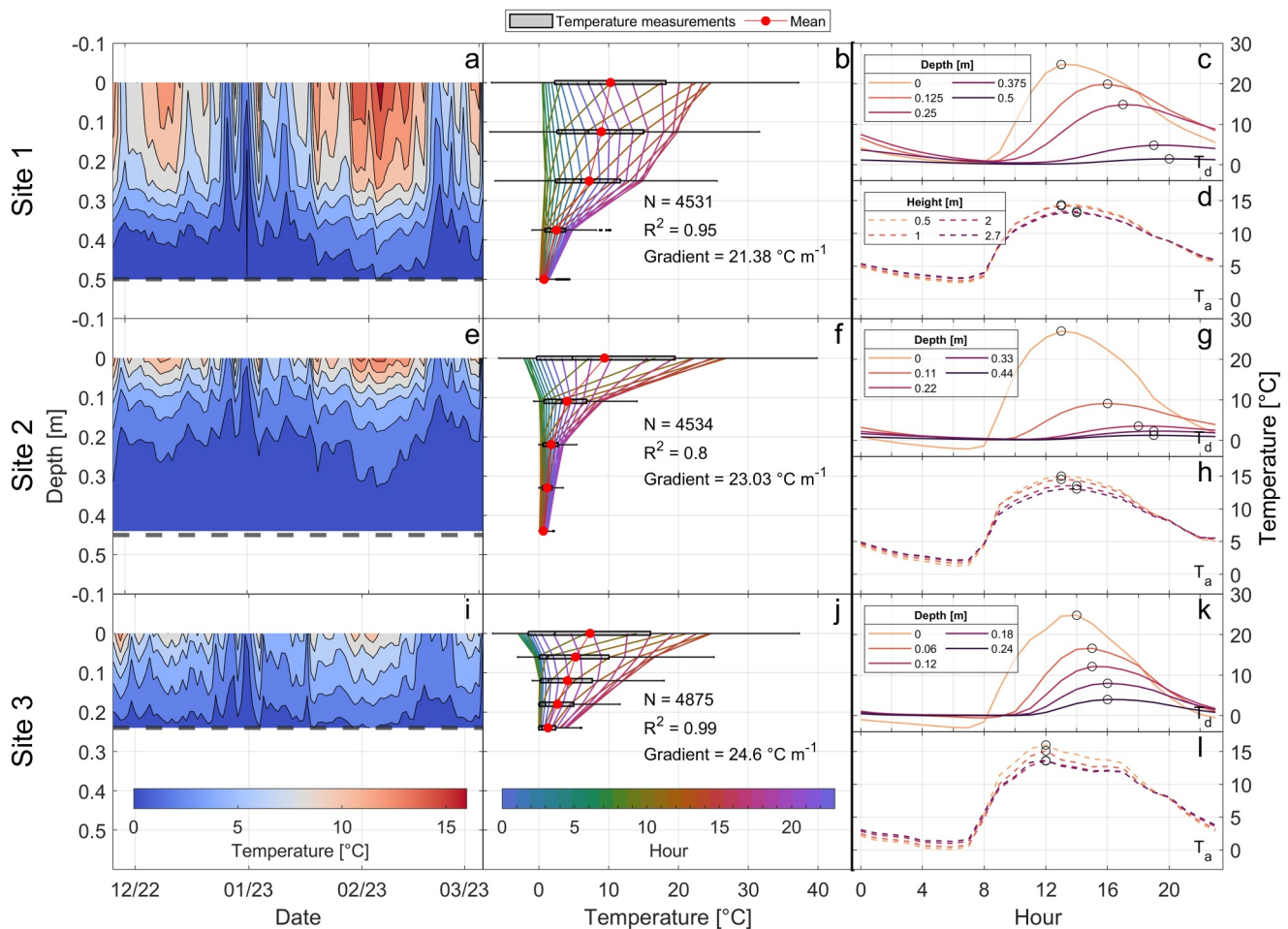


Figure 3. (a, e, i) Daily mean T_d isotherms for the debris layer at each site. (b, f, j) Temperature profiles showing the hourly average temperature and boxplots of the temperature measurements per depth at the three sites. Temperature gradient obtained from a linear regression of the mean temperature as a function of depth. (c, g, k) Debris temperature and (d, h, l) air temperature average diurnal cycles for each depth and height measured, circles indicate the hour at which the maximum is reached.

application, the software automatically identifies the top and bottom of the stake for each picture and the distance between these points is calculated by assigning a scale (10 cm between two marks on the stake). Errors in automated readings (usually overnight or when the light reaching the stake changed) were manually corrected by selecting a point on the bottom or top of the stake, if it had been incorrectly placed. We then converted surface lowering (m) to melt (m w.e.) based on ice density of 917 m⁻³ (Benn & Evans, 2010). Due to the falling of towers 2 and 3, continuous readings were not possible for the entire period. Stakes were also manually measured in March 2023.

2.2.4. Surface Relief

The areas around the towers were surveyed using a DJI Mavic 2 Enterprise quadcopter Unmanned Aerial Vehicle (UAV) at a 12.4 MP resolution, producing 4056 × 3040-pixel RGB images with a fixed 24 mm focal length (35 mm equivalent) and using automatic exposure and focus settings. We then used the structure-from-motion approach to generate DEMs (4 cm ground resolution) with Agisoft Photoscan from the UAV optical imagery (Figure 4a). For details on the structure-from-motion approach workflow, see Westoby et al. (2012), and for specifics on Agisoft, refer to Immerzeel et al. (2014).

The elevation variability of the glacier surface in the area around the towers is shown in Figure 4a. The difference between the lowest and the highest point is 26, 30 and 15 m for sites 1, 2, and 3, respectively, with corresponding standard deviations of 5.8, 5.7, and 2.6 m.

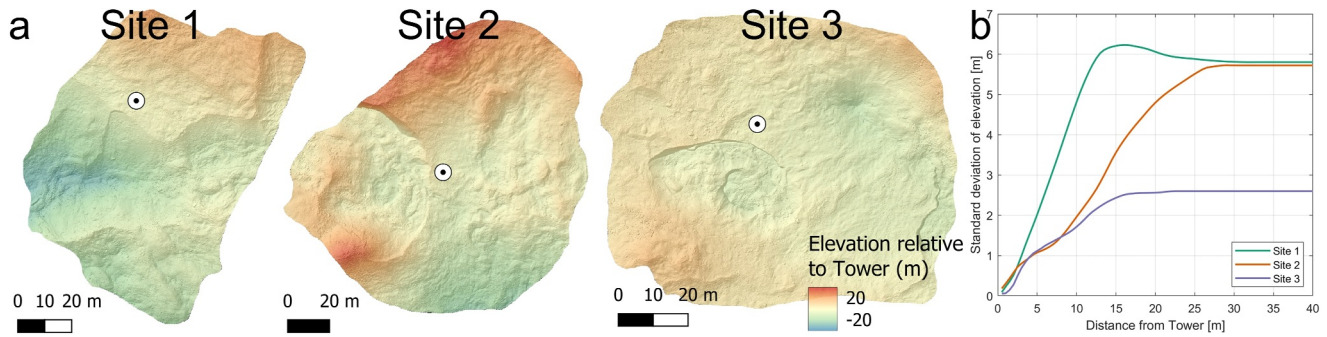


Figure 4. (a) DEMs generated with UAV photogrammetry around the towers (dots) showing the relative elevation compared to the tower location. (b) Standard deviation of elevations around the towers at different distances.

2.3. Methods

2.3.1. Thermal Conductivity

To derive thermal conductivity, we tested four different methods based on the studies of: (a) Nakawo and Young (1982) and Brock et al. (2010), indicated as NYB; (b) Conway and Rasmussen (2000), indicated as CRh; (c) Laha et al. (2022), indicated as CRi; and (d) Fugger et al. (2022), indicated as Opt (Table 3).

2.3.1.1. Nakawo and Young (1982) and Brock et al. (2010)

The thermal conductivity of the debris layer can be calculated as follows:

$$k = \frac{M \cdot L_f \cdot \rho_i \cdot h_d}{(\overline{T_s} - T_{di}) \cdot dt} \quad (1)$$

where M is the cumulative melt over a measurement period (m w.e.), L_f is the latent heat of fusion of ice at 0°C ($334,000 \text{ J kg}^{-1}$), ρ_i is the ice density (kg m^{-3}), h_d is the thickness of the debris layer (m), $\overline{T_s} - T_{di}$ is the mean temperature between the surface (T_s) and the debris-ice interface (T_{di}), in $^\circ\text{C}$, and dt is the duration of the measurement period (s). With this method we calculate a single value for the measurement period for each site.

2.3.1.2. Conway and Rasmussen (2000)

We calculated the thermal diffusivity (κ) of the debris layer using the one-dimensional diffusion equation from measurements of vertical temperature profiles within the debris as follows:

$$\frac{\partial T_d}{\partial t} = \kappa \frac{\partial^2 T_d}{\partial z^2} + s, \quad (2)$$

where T_d is the debris temperature ($^\circ\text{C}$), t is time, z is the depth of the measurement (m) and the term s includes the non-conductive processes. If the system is purely conductive ($s = 0$), then the gradient of the linear regression line provides an estimate of the average κ for depth z and the scatter around the regression indicates non-conductive processes (Figures S8–S10 in Supporting Information S1). To account for the effect of lithological properties, porosity and moisture content, we use Equation 3 (Steiner et al., 2021) to calculate the thermal conductivity from the κ obtained.

$$k = \kappa \left(\rho_r c_r (1 - \phi_d) + \left(\rho_w c_w \frac{\theta}{\theta_{sat}} + \rho_a c_a \left(1 - \frac{\theta}{\theta_{sat}} \right) \right) \phi_d \right) \quad (3)$$

Where ρ , c , and ϕ are density, specific heat capacity and porosity, the subindices r , w , a , and d stand for rock, water, air and debris, respectively, and θ and θ_{sat} are the moisture content and the fully saturated moisture content.

This method yields up to five results per site (one for each thermistor's depth). The top and bottom sensors were excluded from the CRh, as a synthetic experiment showed that those sensors do not perform well (Text S3 in Supporting Information S1).

Due to $\frac{\partial T_d}{\partial t}$ and $\frac{\partial^2 T_d}{\partial z^2}$ having different units, we used normalized total least squares for the regression analysis, and performed the fitting both considering and ignoring the sensor uncertainties. For the top and bottom sensors, single-sided differences were calculated, whereas central differences were calculated for the other sensors. With Equation 2, we calculated κ with $R^2 > 0.5$ and $R^2 > 0.75$, and with these values we obtained the conductivity (k , $\text{W m}^{-1} \text{K}^{-1}$) with Equation 3. We tested values of ρ_r , c_r , ϕ and θ_{sat} from previous studies, as well as estimated values of ρ_r and c_r from field observations. Additionally, we tested calculations with both $\theta = 0$ and $\theta \neq 0$. For the latter one, we used the average value of the measurements of moisture content at each site, for which we considered only the period between the precipitation events of January and February, obtaining moisture content of 0.079, 0.127 and 0.085 $\text{m}^3 \text{m}^{-3}$ for sites 1, 2 and 3, respectively (Figure S12 in Supporting Information S1).

2.3.1.3. Laha et al. (2022)

This method employs the finite-difference approximations shown in Equation 4 to evaluate the derivative terms in Equation 2. It considers higher-order correction terms to be negligible and account for variations in debris thermal properties by using a two-layered model with different thermal diffusivities as follows:

$$\frac{T_d(0, t + \Delta t) - T_d(0, t)}{\Delta t} \approx \frac{\kappa_1 \frac{T_d(-dz_1, t) - T_d(0, t)}{dz_1} - \kappa_2 \frac{T_d(0, t) - T_d(dz_2, t)}{dz_2}}{\frac{dz_1 + dz_2}{2}} \quad (4)$$

where κ_1 and κ_2 represent the thermal diffusivities of the top and bottom layers, with respective thicknesses dz_1 and dz_2 . We applied the method to all the consecutive sets of three thermistors, resulting in up to three values for each site (Figures S13–S15 in Supporting Information S1). We calculated the effective thermal diffusivity of the two layers (κ_{eff}) for each set of thermistors following Laha et al. (2022), as in Equation 5, and then calculated an effective thermal conductivity with Equation 3

$$\frac{h_d}{\kappa_{eff}} = \frac{dz_1}{\kappa_1} + \frac{dz_2}{\kappa_2} \quad (5)$$

We also tested values of ρ_r , c_r , ϕ , and θ_{sat} from previous studies, as well as estimated values of ρ_r and c_r from field observations, and performance metric (R^2 cut-off limit) for the fit of Equation 2.

Since both CRh and CRi yield multiple values per site, a weighted average was calculated using the obtained k values and the following equation:

$$k = \frac{1}{\sum_{i=1}^n \frac{l_i}{k_i}}, \quad (6)$$

where l_i is the thickness of each sub-layer and k_i is the conductivity of each sub-layer.

2.3.1.4. Fugger et al. (2022)

We optimized k by simulating only the conduction of energy through an homogeneous debris cover during snow-free conditions using the one-dimensional heat equation, surface temperature data from the top debris thermistor (near-surface), and ice melt from the ablation stake measurements as the target variable, with the Mean Absolute Error as the performance metric (Figures S16–S18 in Supporting Information S1). We validated these results by comparing the modeled debris temperatures with the debris thermistor data (excluding the top one, since it was used in the optimization process).

2.3.2. Aerodynamic Roughness Length

To derive z_0 , we tested two different methods: (a) Profile aerodynamic method (Chambers et al., 2020; Miles et al., 2017; Quincey et al., 2017; Sicart et al., 2014), indicated as PAM; and (b) Fugger et al. (2022), indicated as Opt (Table 3).

2.3.2.1. PAM

z_0 can be calculated using the tower measurements of temperature with the following equations:

$$u(z) = \frac{u^*}{k} \left(\ln \frac{z+d}{z_0} + \alpha_M \frac{z+d}{L} \right) \quad (7)$$

$$T(z) - T_s = \frac{T^*}{k} \left(\text{Pr} \ln \frac{z+d}{z_T} + \alpha_H \frac{z+d}{L} \right) \quad (8)$$

$$L = \frac{T(u^*)^2}{kgT^*} \quad (9)$$

where, $u(z)$ and $T(z)$ are wind speed (m s^{-1}) and temperature ($^{\circ}\text{C}$) at a height z (m), d is the displacement height from the zero reference level (m), u^* and T^* are the friction velocity and scaling temperature, respectively, z_0 and z_T are the aerodynamic roughness length for momentum and temperature, L is the Monin-Obukhov length, k is the von Kármán constant ($k = 0.4$), α_M and α_H are the bulk stability corrections for momentum and heat (empirically derived coefficients, $\alpha_M = \alpha_H = 5$; Dyer, 1974, Stull, 1988) and the Prandtl number Pr is set to 1 (Brock et al., 2006; Chambers et al., 2020; Miles et al., 2017; Sicart et al., 2014). To derive z_0 we minimized the mismatch between the calculated $\hat{T}(z)$ and $\hat{u}(z)$ (Equations 7–9) and the measured $T(z)$ and $u(z)$ at the towers. That is, we iteratively varied z_0 , z_T , u^* , T^* , and d until $\hat{T}(z)$ and $\hat{u}(z)$ matched $T(z)$ and $u(z)$. We performed the calculations to estimate d and not estimate d (assuming $d = 0$).

$$Ri_b = g \frac{T_z - T_s}{T_0 u^2} (z - z_s) \quad (10)$$

For the stability condition we calculated the Richardson number (Ri_b) as in Equation 10, which describes the stability of the surface layer by relating the effects of buoyancy to mechanical forces (Moore, 1983). In this equation, g is the gravitational constant, $T(z)$ and T_s are the temperatures (K) at height z and at the surface z_s , T_0 is the mean temperature of the air layer (K) and u is the wind speed (m s^{-1}). We used the criteria of $-0.03 < Ri_b < 0.03$ and $u_{2m} \geq 1.5 \text{ m s}^{-1}$ separately (Ri_b and u_{2m}) and combined ($Ri_b u_{2m}$). The surface temperature was not directly measured, but a near-surface temperature was measured with the top thermistor installed next to the tower, which was used as T_s in Equations 7 and 8. Alternatively, we did the calculations replacing T_s by $T_{0.5m}$. As in Chambers et al. (2020), both wind and temperature profiles were fitted simultaneously and iteratively to calculate z_0 , u^* , z_T , T^* , d and L in Equations 7 and 8. To do this, an initial estimate of L is needed, where, following Chambers et al. (2020), we used 10^8 m. With this guess, values for z_0 , u^* , z_T , T^* (and d) were obtained, which were used to calculate a new L (with Equation 9). This sequence is repeated 10 times (Chambers et al., 2020), if the values of L converge, it is assumed that the profiles fit the theory, and they are then used to calculate z_0 , whereas if they did not converge they were discarded.

To estimate the goodness of fit, we used $R^2 > 0.75$ and a goodness-of-fit coefficient (j) that considers the sensor's uncertainties values:

$$\begin{aligned} j_1 &= \sum \left(\frac{\hat{u} - u}{\sigma_u} \right)^2 \\ j_2 &= \sum \left(\frac{\hat{T} - T}{\sigma_T} \right)^2 \\ j &= j_1 + j_2, \end{aligned} \quad (11)$$

where \hat{u} and \hat{T} are the fitted values, u and T are the measured values and σ_u and σ_T are the sensor uncertainties, and the lower j is, the better the fit is. We calculated the z_0 with R^2 and j separately and compared the results. Different combinations of calculations were performed, by (a) using the surface temperature value as the top thermistor (T_s) or the temperature measured at 0.5 m ($T_{0.5m}$), (b) considering or not the temperature and wind sensor uncertainties for the fit, (c) using the data of the entire measurement period for each tower or just the measurement period of tower 3 (the shortest record); (d) using j or R^2 as the performance metric, and (e) considering $d \neq 0$ or $d = 0$.

2.3.2.2. Fugger et al. (2022)

We optimized z_0 after determining the optimized k by running a complete energy-balance melt model, using the surface temperature as the target variable and the Nash–Sutcliffe Efficiency as performance metric (Figures S16–S18 in Supporting Information S1). Since this optimization requires calculation of the full energy mass balance, the required inputs are more than for the optimization of k (for a detailed description of the inputs see Section 2.3.4).

2.3.3. Land-Surface Model Tethys and Chloris

To model sub-debris ice melt rates with the derived debris properties and to estimate the optimized z_0 , we used the energy-balance module of the mechanistic land surface model *Tethys – Chloris* with an hourly time step (*T&C*, Fatichi et al., 2012a, 2012b; Fugger et al., 2022; Mastrotheodoros et al., 2020). The cryospheric components and energy balance routines of *T&C* have been validated in several previous studies (e.g., Buri et al., 2023; Fugger et al., 2022, 2024; Fyffe et al., 2021; Shaw et al., 2022) and the *T&C* energy balance model for snow, ice, and debris-covered ice is detailed in Fyffe et al. (2014) and Fugger et al. (2022). In *T&C*, surface temperature (T_s), the homogeneous radiative temperature of the surface, is determined prognostically at each point. An iterative numerical method calculates all relevant surface energy fluxes, solving for T_s to achieve energy balance closure while simultaneously determining the mass of ice and snow that melts and sublimates (Fyffe et al., 2014). The ice column is represented as a single layer with conduction of energy down to a depth of 2 m, below which it is assumed to be isothermal (Fugger et al., 2022). Transient debris temperature profiles are computed with the heat diffusion equation using numerical methods (Reid & Brock, 2010) and the conductive energy flux at the base of the debris is used for ice melt (Fugger et al., 2022). To estimate the heat transfer between the debris surface and the atmosphere *T&C* uses a resistance analogy scheme (Brutsaert, 2005; Garratt, 1992), where the aerodynamic resistance is based on a simplified Monin-Obukhov solution using a bulk transfer coefficient (Mascart et al., 1995) with aerodynamic, thermal and vapor roughness lengths calculated based on Brutsaert (1982). Accordingly, in *T&C*, the aerodynamic roughness lengths for temperature, water vapor, and momentum are related by the expression $z_{0,T} = z_{0,W} = 0.1z_{0,M}$ (Fugger et al., 2022). Thus, once $z_{0,M}$ is determined as detailed above, the roughness lengths for temperature and vapor can be directly derived.

2.3.4. Input Data and Initial Conditions

T&C requires hourly time series of air temperature (T_{air}), precipitation (Pr), atmospheric pressure (Pre), wind speed (W_s), relative humidity (RH), incoming shortwave radiation (SW_{in}) and incoming longwave radiation (LW_{in}). We used data from AWSs belonging to the Chilean Water Authority (Dirección General de Aguas, DGA) (Figure S19 and Table S3 in Supporting Information S1): the off-glacier AWS (Termas del Plomo, 33.61380°S, 69.90634°W, 3,027 m a.s.l.) has a relatively continuous record since 2016, whereas the on-glacier AWS (Pirámide Glacier, 33.58940°S, 69.89060°W, 3,448 m a.s.l.) has a discontinuous record since 2017. Both stations were used to calculate lapse rates for air and dew point temperature, radiation and atmospheric pressure. ERA5 Land data were used to fill in the gaps after accounting for the calculated lapse rates. T_{air} was distributed using monthly mean lapse rates, while for Pre and SW_{in} an average annual lapse rate was used. For RH the dew temperature was adjusted using lapse rates and then converted to RH . Pr and W_s were assumed to be spatially uniform across the study area at each time step. These lapse rates were used to obtain the forcing variables at the points where ice melt was calculated. Surface albedo was calculated from incoming and outgoing solar radiation at the on-glacier AWS (Figure S20 in Supporting Information S1), with an average albedo of 0.2 over the period of record. For this study, we do not consider spatial variations in surface albedo over the debris. We used the point implementation of the model but accounted for local topographic effects on incoming shortwave radiation, therefore, we required the

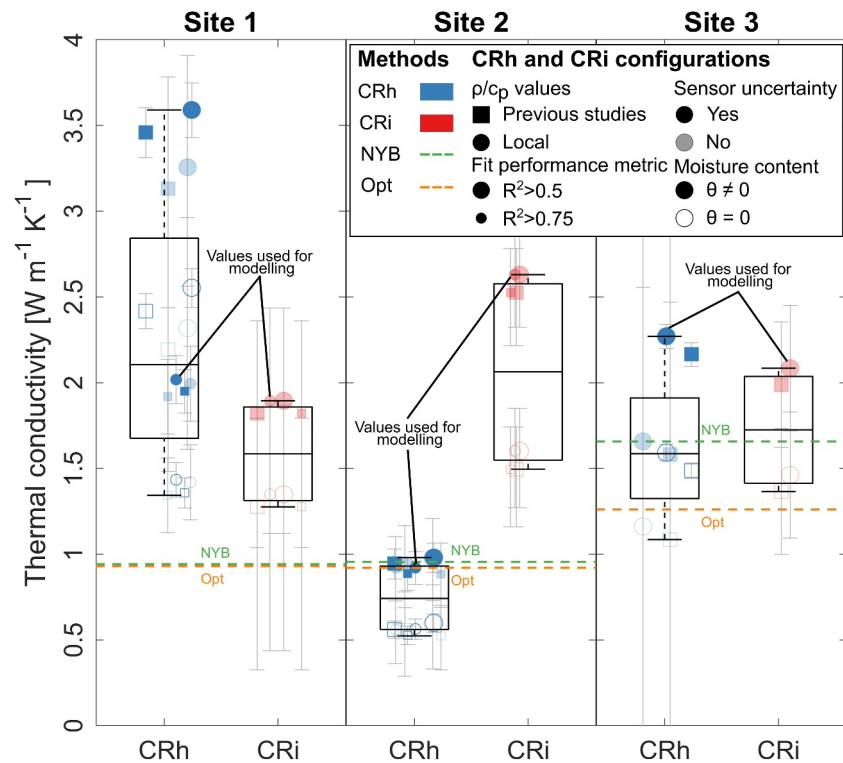


Figure 5. k values obtained with the different variations of CRh and CRi methods (box plots) and the single values yielded by the NYB and Opt methods (horizontal dashed lines).

topography and geometry of the entire glacier. For the topography we used a 12.5 m resolution DEM from the Alaska Satellite Facility. The glacier geometry was extracted from the DGA public glacier inventory (IPG, 2022), and the debris-covered outline was derived from the glacier outline and Google Earth imagery (imagery from 20/01/2023 and 20/05/2023).

2.3.5. Experimental Set-Up

Ice melt at each site was calculated using combinations of k and z_0 and was compared to ablation stake measurements, as well as to ice melt estimates derived using the k and z_0 values reported by Brock et al. (2010), as those are commonly used in previous studies. From all the possible combinations, one value from each method of k and z_0 was selected to simulate and compare sub-debris melt. For CRh and CRi the values used (Figure 5 and Table 4) correspond to the results of the variations that we considered more locally representative, in the sense that they account for more local variables and have a more strict selection criteria: using local ρ_r and c_r values, measured moisture content, sensor uncertainty and $R^2 > 0.75$ (0.5 for CRi). The NYB and the optimization methods only yielded one result per site, thus no choice had to be made. For z_0 using the profile aerodynamic method we selected the variation we considered more locally representative: the one that considered $d \neq 0$, accounted for sensor uncertainty and used the entire measurement period for each tower and the measured T_s (Figure 6 and Table 4). For both parameters, the “more locally representative” is not necessarily the most accurate.

3. Results

3.1. Thermal Conductivity Values

The k values show substantial variability, ranging from 0.93 to 3.59 $\text{W m}^{-1} \text{K}^{-1}$ for site 1, 0.92–2.63 $\text{W m}^{-1} \text{K}^{-1}$ for site 2 and 1.09–2.27 $\text{W m}^{-1} \text{K}^{-1}$ for site 3 (Figure 5). Overall, there is a lack of agreement among the methods, with variations of up to 1.09, 4.05, and 0.82 $\text{W m}^{-1} \text{K}^{-1}$ for site 1, 2 and 3 respectively.

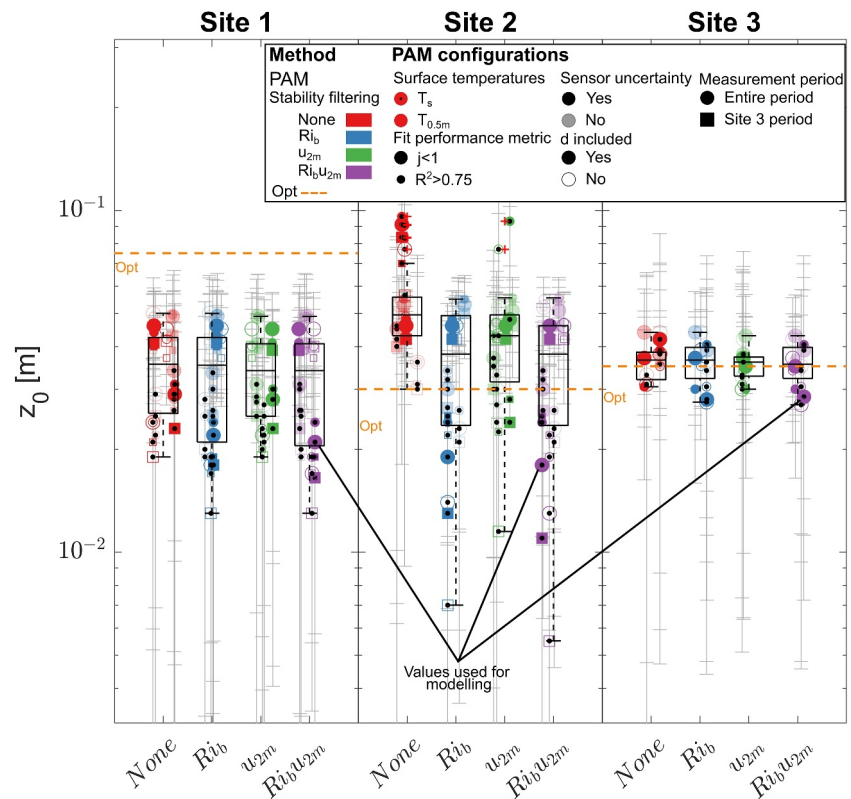


Figure 6. Calculated z_0 values with the different variations of the PAM method considering different filters for stability: None: no stability filtering; Ri_b : Richardson number $<|0.03|$; u_{2m} : wind speed at 2 m $<1.5 \text{ m s}^{-1}$; $Ri_b u_{2m}$: both Ri_b and u_{2m} . For visual clarity, the figure was truncated, as the uncertainty of some results extends beyond the displayed range. The lower bounds of the uncertainty bars are located at 4.3×10^{-5} , 2.3×10^{-4} and 0.019 m for sites 1, 2 and 3, respectively. The results of the Opt method are shown as an orange dashed horizontal line for each site.

At site 1, NYB and Opt methods are in close agreement, whereas the CRh and CRi methods yield higher k . The k obtained with CRh is considerably higher and shows a larger spread among the different variations ($\sim 1.4\text{--}3.6 \text{ W m}^{-1} \text{ K}^{-1}$), whereas CRi yields fewer values (i.e., more results with $R^2 < 0.5$), but with less spread (Figure 5). **At site 2**, when calculating k with CRh and including the moisture content ($\theta \neq 0$), the results are similar to both NYB and Opt. However, all CRi results are higher than NYB and Opt results. **At site 3**, as opposed to the other ones, the results of NYB and Opt differ. This site has very few valid values for the CRh/CRi methods (as most calculations resulted in $R^2 < 0.5$), but both CRh and CRi give relatively similar results, with median values close to the NYB value and most results higher than the Opt value. Since NYB, CRh, and Opt agree at site 2, we analyzed the temperature profiles of the other sites to identify time windows where their behavior was similar to the profiles at site 2. We then tested these time windows for the k calculations to see if the results agreed more. However, these calculations yielded fewer and less consistent results across all sites, with k values changing both in number and value simply by taking a subset of the original data, highlighting the methods' sensitivity to input data.

With all variations calculated for the CRh and CRi methods we can analyze how these methods are affected by changes in ρ_r and c_r , sensor uncertainty, moisture content and performance metric cut-off. Both methods show a greater dependence on the inclusion of moisture content compared to any of the other variables, with the exception of site 1, where the change between using $R^2 > 0.75$ and $R^2 > 0.5$ has a similar impact to the moisture content. Including the moisture in the calculations increases the resulting k value in all cases (Figure 5 and Table S4 in Supporting Information S1), with mean increases of 0.79, 0.37 and $0.59 \text{ W m}^{-1} \text{ K}^{-1}$ for sites 1, 2 and 3, respectively. In our case, the debris lithology does not significantly affect the derived k value, as the three sites have relatively similar lithological compositions (Text S2 in Supporting Information S1). However, considering that the debris cover lithological units can change significantly in small areas (Figure 1), in glaciers where lithologies vary more drastically, debris composition could have a greater influence on thermal conductivity.

Previous studies on aerodynamic roughness length of debris-covered glaciers have demonstrated its variability in response to meteorological conditions (e.g., Quincey et al., 2017). Similarly, changes in thermal conductivity values over time have been observed (e.g., Nicholson & Benn, 2012). Despite this, many studies often use a single value for prolonged periods. Given that our results indicate a strong influence of moisture on the derived k values, we investigated whether our k estimates vary over time and explored potential links to meteorological conditions. Daily k values calculated using CRh and CRi variations (Figure S21 in Supporting Information S1) show significant variability. CRh is particularly sensitive to precipitation events, leading to unstable and elevated k values during wet periods compared to drier conditions. In contrast, CRi does not seem to show the same dependency, with values across sites showing less consistent stabilization. We therefore explored the effect of subdividing the data into “wet” periods, defined as precipitation events and up to two days afterward, and “dry” periods, defined as the intervals between precipitation events (Figure S22 and Table S5 in Supporting Information S1). Our results remain relatively unchanged when comparing the overall results with the dry periods (absolute change between $\sim 0.007\text{--}0.08\text{ W m}^{-1}\text{ K}^{-1}$ for CRh and $\sim 0.005\text{--}0.04\text{ W m}^{-1}\text{ K}^{-1}$ for CRi), whereas, when comparing with the wet periods CRh shows a more substantial increase between 0.3 and $0.6\text{ W m}^{-1}\text{ K}^{-1}$ and CRi an increase between 0.05 and $0.6\text{ W m}^{-1}\text{ K}^{-1}$.

3.2. Aerodynamic Roughness Length Values

Aerodynamic roughness length values range from 0.013 to 0.075 m , from 0.005 to 0.096 m and from 0.027 to 0.05 m in sites 1, 2 and 3, respectively (Figure 6). **At site 1**, the PAM values are lower than the Opt ones, and the different stability filters do not have a large impact on the results. **At site 2**, the value of the Opt method is within the range of the PAM results, there is a greater spread of values and filtering has a larger impact than at site 1. Finally, **at site 3**, the median value of the PAM results are in good agreement with the Opt results, there is little spread among all the variations and the different filtering methods do not considerably affect the end result.

Using all variations calculated for the PAM method, we can evaluate how the method responds to changes in T_s , d , sensor uncertainty, measurement period and performance metric cut-off. Using T_s instead of $T_{0.5m}$ has the greatest impact at all three sites, always decreasing the final z_0 value. This is followed in importance by the time period used at sites 1 and 2, where using the shorter measurement period of site 3 increases z_0 (Figure 6 and Table S6 in Supporting Information S1).

Aerodynamic roughness length is also variable in time as surface conditions change (Quincey et al., 2017), and the PAM method is usually used to obtain one representative value or a range of values for each glacier (e.g., Chambers et al., 2020; Sicart et al., 2014). We calculated daily values of z_0 using the selected variation of PAM (Figure S23 in Supporting Information S1) and examined whether the derived values show temporal changes, as well as whether these variations correlate with local meteorology. The three sites exhibit significant variability over the measurement period, although the variation does not show a clear correlation with temperature or wind speed/direction variability (data used for the calculations) during this period.

3.3. Modeled Ablation

The simulated ice melt using different combinations of k and z_0 ranges widely, and in some cases differs substantially from ice melt observed at the ablation stakes (Table 5 and Figure 7).

When modeling ice melt with the debris properties reported by Brock et al. (2010), the modeled ice melt does not align with the measurements. Furthermore, using the k values calculated with the CRh, CRi and NYB methods, the modeled ice melt generally does not match the measurements, with the exception of the values calculated using the CRh method on site 2 and the NYB method on site 1 (Table 5 and Figure 7). When examining the effect of the values of k and z_0 on the simulated melt, it can be seen that the final ice melt is more dependent on the choice of method for calculating k . For example, at site 2, when calculating ice melt with CRi/PAM and CRi/Opt (keeping the k method constant) the difference of ice melt is $<2\%$, whereas when calculating with CRi/PAM and Opt/PAM (keeping the z_0 method constant), the difference is 66% (Table 5). When looking at the modeled surface temperature, the results are similar to the ice melt (Figure S24 in Supporting Information S1).

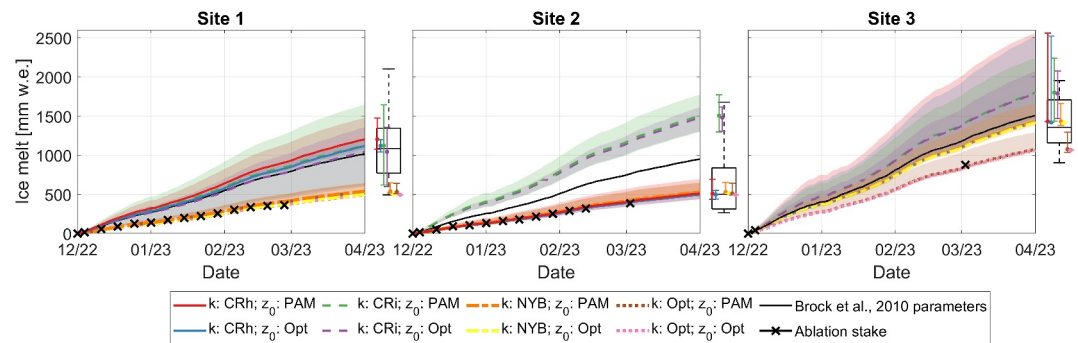


Figure 7. Modeled and measured ice melt at the three sites. The shaded areas represent the melt modeled using the uncertainties of k and z_0 . The combination of the selected values (Table 4) for each method are plotted as colored lines, the commonly used values in previous studies (Brock et al., 2010) as a black line and measured ablation as black crosses (plotted only once a week for visualization purposes). Box plots of all the combinations are shown to the right of each plot.

4. Discussion

4.1. Thermal Conductivity Estimates

4.1.1. CRh and CRi

CRh explicitly considers debris properties such as ρ_r , c_r , ϕ and θ , particularly with Equation 3. Given that this method is based on the one-dimensional diffusion equation, it would perform the best under conditions where $\frac{\partial T}{\partial t} = 0$, the system is entirely conductive, and conductivity is constant with depth (Conway & Rasmussen, 2000). Yet, these conditions are uncommon in porous materials like supraglacial debris, where energy transfer involves multiple processes (Farouki, 1981; Humlum, 1997). Variations in moisture content, lithology and porosity can cause depth-dependent variations in k (Conway & Rasmussen, 2000; Nicholson & Benn, 2012; Steiner et al., 2021). CRi addresses debris layer heterogeneity with a two-layered model, yet it also performs best under conditions where $\frac{\partial T}{\partial t} = 0$ and the system is purely conductive. The linear regressions with higher R^2 values usually correspond to positions lower in the debris layer, where non-conductive processes are less prevalent (Figure S25 in Supporting Information S1).

The variation in the methods' performance may relate to the debris layer structure. Despite similar debris thickness and ice melt between sites 1 and 2, site 1 exhibits significantly higher k values with CRh and CRi compared to NYB and Opt. The debris layer structure at the two sites is very different: at site 1, a thin layer of wet fine debris sits beneath a thick layer of dry large debris; while at site 2 a thicker layer of wet fine debris is beneath a thinner layer of dry large debris. This is also evident in the shape of the daily temperature profiles within the debris (Figures 3b–3f and 3j). At site 1, where a large proportion of the debris consists of medium-to large-sized clasts (Figure S26 in Supporting Information S1), the temperature profiles show a wider spread between the surface and approximately 30 cm depth. In contrast, at site 2, which a lower proportion of medium and large clasts, the wider temperature distribution is limited to the upper ~ 10 cm of the debris layer. This distinct layering might explain the higher k value at site 1 (Figure S26 in Supporting Information S1): The thicker large debris layer at site 1 impacts CRh and CRi, since it contains air pockets between large clasts, which could facilitate convection. Figure 5 and Table S4 in Supporting Information S1 supports this hypothesis, with an increased R^2 cut-off threshold notably impacting k values at site 1, which we interpret to indicate a larger non-conductive processes term (Conway & Rasmussen, 2000; Nicholson & Benn, 2012; Petersen et al., 2022). CRh and CRi at site 3 show values generally higher than Opt and median values similar to NYB, but this site is dominated by wet fine debris, which may enhance heat advection through water transport, and the debris thickness at this site falls below recent literature recommendations (Beck & Nicholson, 2023).

Our results indicate that moisture within the debris significantly influences k , particularly during wet periods following precipitation events. While individual k estimates are site-specific and reflect localized conditions within the debris layer, fluctuations in these values may indicate changes in the bulk k , which integrates the effects of all physical processes across the debris layer.

Temporal and spatial sampling intervals, sensor uncertainty, and errors in debris thermistor depth can alter the calculated k . Beck and Nicholson (2023) recommend using thermistors with a precision of 0.1°C, a debris layer depth of at least 40 cm, three thermistors spaced 8–20 cm apart, high temporal resolution, then average over a 5 min period, and stable, dry meteorological conditions for at least a week. We were able to implement most of their recommendations, except for the high temporal resolution, which could be a contributing factor to the disagreement between methods.

4.1.2. NYB and Opt

NYB assumes minimal change in heat stored in the debris layer over time and a linear vertical temperature gradient (Brock et al., 2010), generally acceptable for periods exceeding a week (Conway & Rasmussen, 2000; Nicholson & Benn, 2006). However, hourly temperature gradients may not always be linear, revealing varied profile patterns (Figures 3b–3f and 3j). Despite a higher linearity at site 3 ($R^2 = 0.99$), NYB results differ most there from Opt, which best reproduces the observed ablation. NYB uses only surface and ice-debris interface temperatures and ablation data, neglecting debris layer characteristics. The advantage lies in calculating bulk k (required by energy-balance models), acknowledging heat transport complexities such as convection, evaporation and percolation of rainwater (Brock et al., 2010). In contrast, the CRh and CRi methods rely on linear regressions, which often have higher R^2 values at lower debris depths where non-conductive processes are less significant. As a result, these depths are used in the calculation of k , while depths with lower R^2 are excluded, which biases the k values obtained to be representative of the lower layers. This can lead to a mismatch between the local k values derived in this way and the “bulk” thermal conductivity required for models, as the latter has to integrate the effects of all physical processes throughout the debris layer.

We examined how the NYB and Opt methods are affected by the measurement period by analyzing sub-periods (>week) of ablation and temperature data, comparing them to results from the entire period (Figure S27 in Supporting Information S1). The findings indicate differences within ranges of –24% to 12% (NYB) and –42% to 5% (Opt) for site 1, $\pm 20\%$ (NYB) and $\pm 30\%$ (Opt) for site 2, and –36% (NYB) and 0% (Opt) for site 3, highlighting their high dependency on the length of the measurement period.

4.2. Aerodynamic Roughness Length Estimates

The PAM method relies on assumptions that hold true only under an idealized surface boundary layer that is horizontal, homogeneous and in steady-state conditions. Filtering measured data to ensure a good fit and satisfy theoretical assumptions drastically reduces the number of valid profiles, which represent only a small fraction of the measurement period at each site (Table 2). Nonetheless, profile fits with and without filtering yield generally similar values, as observed in previous studies Figure 6; Sicart et al., 2014).

The application of Monin-Obukhov similarity theory assumes the presence of a homogeneous upwind area with consistent aerodynamic properties, which is rarely the case for debris-covered glaciers (Chambers et al., 2020; Miles et al., 2017), and is also not observed at our study sites except for site 3, which exhibits relatively homogeneous terrain around the tower (Figure 4a). Variability in elevation around the tower increases rapidly with distance for sites 1 and 2, whereas site 3 shows a slower increase. At 30 m from the towers, site 3 demonstrates less than half the standard deviation of sites 1 and 2 (2.6 vs. 5.8 and 5.8; Figure 4b).

The hummocky nature of debris-covered glaciers and the debris surface's ability to regulate temperature (Evatt et al., 2015) significantly complicate the implementation of Monin-Obukhov theory (Miles et al., 2017). The large hummocks and troughs combine to create an unstable and heterogeneous roughness layer (Shao & Yang, 2008), and the underlying viscous sublayer, which is regulated by roughness elements at the microtopographic scale, may limit turbulent energy transfer to the surface (Smeets & Broeke, 2008).

4.3. Limitations and Recommendations

Because of sampling biases in our experimental setting, our derived values may or may not represent the broader glacier domain. The towers were placed in relatively flat areas along the glacier's central line, where debris thickness ranged from 24 to 50 cm, allowing for easier placement of thermistors with reasonable spacing.

Table 2

Number of Profiles and Percentage of the Total Profile Count After Filtering the Calculations Using the Measured Surface Temperature With the Top Debris Thermistor, Considering $d \neq 0$, Sensor Uncertainty and the Entire Measuring Period of Each Tower

	Site 1		Site 2		Site 3	
	Number	%	Number	%	Number	%
All profiles	4,299	100	3,851	100	607	100
Ri _b filter	1,890	44	1,331	35	132	22
u _{2m} filter	3,443	80	2,441	63	386	64
Ri _b u _{2m} filter	1,731	40	1,288	33	107	18
L convergence, $j < 1$	572	13	290	8	54	9
L convergence, $R^2 > 0.75$	358	8	174	5	26	4

Although site selection did not explicitly account for variations in parameters affecting k (e.g., lithology and moisture content), our results represent some variability across the glacier surface. This variability might not cover the full range of values at the site but is illustrative. Few studies have reported multiple and simultaneous (or within the same year) measurements of conductivity at different glacier locations (Anderson et al., 2021; Conway & Rasmussen, 2000; Rounce et al., 2015). These studies show similar ranges of variability (~ 0.4 – $1.2 \text{ W m}^{-1} \text{ K}^{-1}$), highlighting that a single value may not be suitable for any site. Notably, in our case, the NYB and Opt methods produced consistent values for sites 1 and 2 (NYB: 0.94 and $0.95 \text{ W m}^{-1} \text{ K}^{-1}$; Opt: 0.93 and $0.92 \text{ W m}^{-1} \text{ K}^{-1}$, respectively).

For the z_0 results, we obtain ranges of approximately one order of magnitude (0.018 – 0.0285 m for PAM and 0.03 – 0.075 m for Opt). Unfortunately, to the best of our knowledge, no other studies use multiple wind-temperature towers to estimate z_0 , but we can compare this range with that estimated by Miles

et al. (2017) with the microtopographic method on Lirung Glacier (Nepal), which obtained results varying at least 3 orders of magnitude across the glacier. Considering this, our results from the three towers in Pirámide Glacier are clustered around the established values for a debris-covered glacier (Brock et al., 2010; Miles et al., 2017), but may not represent the full range of possible values.

The discrepancies observed between the methods also highlight the need for caution when relying on assumed or previously published values for debris properties. Given the variability encountered between sites and approaches, it becomes important to reconsider the validity and applicability of such values in modeling sub-debris ice melt with energy-balance models or in the estimation of debris thickness (e.g., Buri et al., 2023; Fugger et al., 2022; McCarthy et al., 2022; Rounce et al., 2018; Rounce et al., 2021). Revisiting previous studies that derive these properties from one method and analyzing them with alternative methods or parameters could be informative both to analyze the transferability of our findings and to verify previous results. This re-evaluation could provide insights into the robustness of previous results and lead to more accurate assessments of parameter uncertainty in future research.

For energy-balance modeling of debris-covered glaciers, deriving a k value by optimizing it against measured ice melt with observed surface temperature data appears to be the most viable approach. This method requires less field data and provides the bulk value that the energy-balance model requires. Its transferability to other

Table 3

Summary of Methods Used for k and z_0 Derivation

Method	Description
Thermal conductivity	
NYB (Nakawo & Young, 1981, 1982)	From ablation measurements and assuming a linear mean vertical temperature gradient
CRh (Conway & Rasmussen, 2000)	Based on the one-dimensional diffusion equation, assuming a heterogeneous debris layer, multiple thermistors at different depths and calculating the temporal and spatial derivatives
CRi (Laha et al., 2022)	Based on CRh, but generalized to a two-layered model to account for inhomogeneities
Opt (Fugger et al., 2022)	Optimisation by simulating conduction through a homogeneous debris cover with surface temperature and ablation as the target variables
Aerodynamic roughness length	
PAM (e.g., Sicart et al., 2014)	Profile Aerodynamic Method: derives z_0 from wind and temperature towers, based on the Monin-Obukhov similarity theory, which is only valid for a near-neutral surface boundary layer
Opt (Fugger et al., 2022)	Optimisation of the energy balance, following the determination of k with the Opt method

Table 4
k and z_0 Values Used for the Ice Melt Simulations for Each Site

Thermal conductivity									
Site	Method	ρ	c_p	Range of R^2 of the fits	Sensor uncertainty	Moisture	# Of <i>k</i> values	$k [W m^{-1} K^{-1}]$	$\sigma [W m^{-1} K^{-1}]$
1	CRh	2,685	796.9	0.79	Yes	Yes	1	2.02	± 0.13
	CRi	2,685	796.9	0.8 – 0.85	–	Yes	3	1.89	+0.54/ – 0.77
	NYB	–	–	–	–	–	–	0.94	–
	Opt	2,685	796.9	–	–	–	–	0.93	–
2	CRh	2,657	816.1	0.75 – 0.87	Yes	Yes	2	0.92	+0.09/ – 0.1
	CRi	2,657	816.1	0.79 – 0.89	–	Yes	3	2.63	+0.26/ – 0.31
	NYB	–	–	–	–	–	–	0.95	–
	Opt	2,657	816.1	–	–	–	–	0.92	–
3	CRh	2,658	815.6	0.52 – 0.58	Yes	Yes	2	2.27	± 0.07
	CRi	2,658	815.6	0.64	–	Yes	1	2.08	± 0.37
	NYB	–	–	–	–	–	–	1.66	–
	Opt	2,658	815.6	–	–	–	–	1.26	–
Aerodynamic roughness length									
Site	Method	T_s	Performance metric	Sensor uncertainty	d	Period	$z_0 [m]$	NMAD [m]	
1	PAM	T_s	$j < 1$	Yes	Yes	Full	0.021	0.0198	
	Opt	–	–	–	–	–	0.075	–	
2	PAM	T_s	$j < 1$	Yes	Yes	Full	0.018	0.0176	
	Opt	–	–	–	–	–	0.03	–	
3	PAM	T_s	$j < 1$	Yes	Yes	Full	0.0285	0.03	
	Opt	–	–	–	–	–	0.035	–	

sub-debris conduction models (e.g., Evatt et al., 2015; Reid & Brock, 2010) remains to be seen, but it should produce a similar bulk estimate for most models due to similar assumptions. While optimized *k* values can improve model performance for the specific data set and conditions used, they may not represent universally applicable or physically accurate values, given that other factors (e.g., aerodynamic roughness length, albedo, or debris moisture content) could partially compensate for inaccuracies in *k*. The choice of method and configuration for determining z_0 is less critical compared to thermal conductivity since it has a smaller impact on total ice melt. While optimizing for *k* only involves simulating conduction through the debris, optimizing for z_0 requires running the entire energy-balance model, making it model-dependent. Despite the higher economic cost of measurements for PAM compared to Opt, the latter remains independent of ice melt calculations and is therefore preferable.

5. Conclusions

This study analyses established methods for deriving thermal conductivity and aerodynamic roughness length for debris-covered glaciers from field measurements and assesses the impact the results have when applying an energy-balance model to calculate ice melt at the point scale.

Our analysis of the effect of changing moisture content, sensor uncertainty, performance metric cut-off, and lithological parameters revealed that methods for estimating thermal conductivity using the diffusivity equation (CRh and CRi) were most affected by changes in moisture content. Additionally, the CRh calculations were notably affected by increases in moisture content resulting from precipitation events. The profile aerodynamic method for estimating aerodynamic roughness length showed more dependence on surface temperature, followed by the measurement period used.

Table 5
Total Modeled Ice Melt ($Ice\ melt_{Mod}$) at the Three Sites Over the Modeling Period, December 2022 to April 2023 and Over the Ablation Stake Measuring Period, Compared With the Observed Ice Melt From the Ablation Stakes ($Ice\ melt_{Obs}$)

Site	k method	z_0 method	k [$W\ m^{-1}\ k^{-1}$]	z_0 [m]	Ice melt _{Mod} (modeling period) [mm w.e.]	Ice melt _{Mod} (ablation stake measuring period) [mm w.e.]	Ice melt _{Obs} [mm w.e.]
1	CRh	PAM	2.02	0.021	1,203	960	390
		Opt	2.02	0.075	1,118	880	
	CRi	PAM	1.89	0.021	1,122	896	
		Opt	1.89	0.075	1,043	820	
	NYB	PAM	0.94	0.021	539	433	
		Opt	0.94	0.075	499	394	
		PAM	0.93	0.021	532	427	
		Opt	0.93	0.075	493	389	
2	CRh	PAM	0.92	0.018	510	409	384
		Opt	0.92	0.03	496	395	
	CRi	PAM	2.63	0.018	1,503	1,189	
		Opt	2.63	0.03	1,479	1,164	
	NYB	PAM	0.95	0.018	529	424	
		Opt	0.95	0.03	514	409	
		PAM	0.92	0.018	509	408	
		Opt	0.92	0.03	494	394	
3	CRh	PAM	2.27	0.029	1,430	1,125	877
		Opt	2.27	0.035	1,418	1,113	
	CRi	PAM	2.08	0.029	1,799	1,411	
		Opt	2.08	0.035	1,787	1,398	
	NYB	PAM	1.66	0.029	1,430	1,124	
		Opt	1.66	0.035	1,417	1,112	
		PAM	1.26	0.029	1,075	849	
		Opt	1.26	0.035	1,065	839	

Note. The gray cells are the modeled results that are within $\pm 10\%$ of the observed melt for each site.

We find that:

- There is a lack of consistent agreement between the different methods of deriving both thermal conductivity and aerodynamic roughness length, leading to a large range of values depending on the approach, experimental set-up, and assumptions. Discrepancies often arise between the ice melt results from energy-balance calculations and the observed data from ablation stakes when using established methods. These inconsistencies highlight the substantial impact that the chosen method can have on the modeled ice melt.
- For the purpose of energy-balance modeling of debris-covered glaciers, optimizing thermal conductivity values against measured ice melt with observed surface and debris/ice interface temperature data appears to be a viable method to constrain melt simulations. It requires less field data, it is independent of the energy-balance model structure and associated limitations, and it provides a bulk value.
- The selection of a method to determine the aerodynamic roughness length is less critical at this glacier during the study period, since it has a smaller impact on total ice melt. Moreover, optimizing for aerodynamic roughness length is dependent on the energy-balance model. Despite the higher economic cost associated with measurements for the profile aerodynamic method compared to optimization, they remain entirely independent of ice melt calculations and might thus be preferable.

This study highlights the challenges and limitations of existing methods in determining thermal conductivity and aerodynamic roughness length on debris-covered glaciers, revealing large and unexpected differences between existing methods. This identified knowledge gap has implications for modeling ice melt and understanding energy-balance processes on debris-covered glaciers. Therefore, it should be addressed by the community.

Data Availability Statement

Available at the following link: <https://doi.org/10.5281/zenodo.11581073> (Melo Velasco et al., 2024), are all the data sets and codes for calculating thermal conductivity and aerodynamic roughness length at the three sites.

Acknowledgments

This project received funding from the Swiss National Science Foundation (Grant 204322, project “REsolving the thickNess Of debris on Earth’s glaciers and its Rate of change,” RENOIR). We thank Lars Groeneveld, Diego Hernández, Alonso Mejías, Gabriela Reyes and Gabriela Tala for their support during fieldwork. Open access funding provided by Institute of Science and Technology Austria/KEMÖ.

References

- Anderson, L. S., & Anderson, R. S. (2016). Modeling debris-covered glaciers: Response to steady debris deposition. *The Cryosphere*, 10(3), 1105–1124. <https://doi.org/10.5194/tc-10-1105-2016>
- Anderson, L. S., & Anderson, R. S. (2018). Debris thickness patterns on debris-covered glaciers. *Geomorphology*, 311, 1–12. <https://doi.org/10.1016/j.geomorph.2018.03.014>
- Anderson, L. S., Armstrong, W. H., Anderson, R. S., & Buri, P. (2021). Debris cover and the thinning of Kennicott Glacier, Alaska: In situ measurements, automated ice cliff delineation and distributed melt estimates. *The Cryosphere*, 15(1), 265–282. <https://doi.org/10.5194/tc-15-265-2021>
- Ayala, A., Pellicciotti, F., MacDonell, S., McPhee, J., Vivero, S., Campos, C., & Egli, P. (2016). Modelling the hydrological response of debris-free and debris-covered glaciers to present climatic conditions in the semi-arid Andes of central Chile. *Hydrological Processes*, 30(22), 4036–4058. <https://doi.org/10.1002/hyp.10971>
- Beck, C., & Nicholson, L. (2023). Numerical study of the error sources in the experimental estimation of thermal diffusivity: An application to debris-covered glaciers. *EGU sphere (November)*, 1–24. <https://doi.org/10.5194/egusphere-2023-2766>
- Benn, D., & Evans, D. J. A. (2010). *Glaciers and glaciation, 2nd edition* (2nd ed.). Routledge. <https://doi.org/10.4324/9780203785010>
- Boisier, J. P., Rondanelli, R., Garreaud, R. D., & Muñoz, F. (2016). Anthropogenic and natural contributions to the Southeast Pacific precipitation decline and recent megadrought in central Chile. *Geophysical Research Letters*, 43(1), 413–421. <https://doi.org/10.1002/2015GL067265>
- Brock, B. W., Mihalcea, C., Kirkbride, M. P., Diolaiuti, G., Cutler, M. E., & Smiraglia, C. (2010). Meteorology and surface energy fluxes in the 2005–2007 ablation seasons at the Miage debris-covered glacier, Mont Blanc Massif, Italian Alps. *Journal of Geophysical Research*, 115(9). <https://doi.org/10.1029/2009JD013224>
- Brock, B. W., Willis, I. C., & Sharp, M. J. (2006). Measurement and parameterization of aerodynamic roughness length variations at Haut Glacier d’Arolla, Switzerland. *Journal of Glaciology*, 52(177), 281–297. <https://doi.org/10.3189/172756506781828746>
- Brutsaert, W. (1982). *Evaporation into the atmosphere*. Springer Netherlands. <https://doi.org/10.1007/978-94-017-1497-6>
- Brutsaert, W. (2005). *Hydrology: An introduction*. Cambridge University Press. <https://doi.org/10.1017/CBO9780511808470>
- Burger, F., Ayala, A., Farias, D., Shaw, T. E., MacDonell, S., Brock, B. W., et al. (2018). Interannual variability in glacier contribution to runoff from a high-elevation Andean catchment: Understanding the role of debris cover in glacier hydrology. *Hydrological Processes*, 33(2), 214–229. <https://doi.org/10.1002/hyp.13354>
- Buri, P., Faticchi, S., Shaw, T. E., Miles, E. S., McCarthy, M. J., Fyffe, C. L., et al. (2023). Land surface modeling in the Himalayas: On the importance of evaporative fluxes for the water balance of a high-elevation catchment. *Water Resources Research*, 59(10). <https://doi.org/10.1029/2022WR033841>
- Chambers, J. R., Smith, M. W., Quincey, D. J., Carrivick, J. L., Ross, A. N., & James, M. R. (2020). Glacial aerodynamic roughness estimates: Uncertainty, sensitivity, and precision in field measurements. *Journal of Geophysical Research: Earth Surface*, 125(2). <https://doi.org/10.1029/2019JF005167>
- Compagno, L., Huss, M., Miles, E. S., McCarthy, M. J., Zekollari, H., Dehecq, A., et al. (2022). Modelling supraglacial debris-cover evolution from the single-glacier to the regional scale: An application to high Mountain Asia. *The Cryosphere*, 16(5), 1697–1718. <https://doi.org/10.5194/tc-16-1697-2022>
- Conway, H., & Rasmussen, L. A. (2000). *Summer temperature profiles within supraglacial debris on Khumbu Glacier* (Vol. 264, pp. 89–97). IAHS-AISH Publication.
- Dyer, A. J. (1974). A review of flux-profile relationships. *Boundary-Layer Meteorology*, 7(3), 363–372. <https://doi.org/10.1007/BF00240838>
- Evatt, G. W., Abrahams, I. D., Heil, M., Mayer, C., Kingslake, J., Mitchell, S. L., et al. (2015). Glacial melt under a porous debris layer. In *Journal of Glaciology* (Vol. 61(229), pp. 825–836). International Glaciology Society. <https://doi.org/10.3189/2015JG14235>
- Falvey, M., & Garreaud, R. D. (2009). Regional cooling in a warming world: Recent temperature trends in the southeast Pacific and along the west coast of subtropical South America (1979–2006). *Journal of Geophysical Research*, 114(4). <https://doi.org/10.1029/2008JD010519>
- Farouki, O. (1981). *Thermal properties of soils (Tech. Rep.)*. U.S. Army Cold Regions Research and Engineering Laboratory.
- Faticchi, S., Ivanov, V. Y., & Caporali, E. (2012a). A mechanistic ecohydrological model to investigate complex interactions in cold and warm water-controlled environments: 1. Theoretical framework and plot-scale analysis. *Journal of Advances in Modeling Earth Systems*, 4(5), 1–31. <https://doi.org/10.1029/2011MS000086>
- Faticchi, S., Ivanov, V. Y., & Caporali, E. (2012b). A mechanistic ecohydrological model to investigate complex interactions in cold and warm water-controlled environments: 2. Spatiotemporal analyses. *Journal of Advances in Modeling Earth Systems*, 4(5), 1–22. <https://doi.org/10.1029/2011MS000087>
- Fischer, L., Huggel, C., Kääh, A., & Haerberli, W. (2013). Slope failures and erosion rates on a glacierized high-mountain face under climatic changes. *Earth Surface Processes and Landforms*, 38(8), 836–846. <https://doi.org/10.1002/esp.3355>
- Fugger, S., Fyffe, C. L., Faticchi, S., Miles, E. S., McCarthy, M., Shaw, T. E., et al. (2022). Understanding monsoon controls on the energy and mass balance of glaciers in the Central and Eastern Himalaya. *The Cryosphere*, 16(5), 1631–1652. <https://doi.org/10.5194/tc-16-1631-2022>
- Fugger, S., Shaw, T. E., Jouberton, A., Miles, E. S., Buri, P., McCarthy, M. J., et al. (2024). Hydrological regimes and evaporative flux partitioning at the climatic ends of High Mountain Asia. *Environmental Research Letters*, 19(4), 044057. <https://doi.org/10.1088/1748-9326/ad25a0>
- Fujita, K., & Sakai, A. (2014). Modelling runoff from a Himalayan debris-covered glacier. *Hydrology and Earth System Sciences*, 18(7), 2679–2694. <https://doi.org/10.5194/hess-18-2679-2014>
- Fyffe, C. L., Potter, E., Fugger, S., Orr, A., Faticchi, S., Loarte, E., et al. (2021). The energy and mass balance of Peruvian glaciers. *Journal of Geophysical Research: Atmospheres*, 126(23), 1–22. <https://doi.org/10.1029/2021JD034911>
- Fyffe, C. L., Reid, T. D., Brock, B. W., Kirkbride, M. P., Diolaiuti, G., Smiraglia, C., & Diotri, F. (2014). A distributed energy-balance melt model of an alpine debris-covered glacier. *Journal of Glaciology*, 60(221), 587–602. <https://doi.org/10.3189/2014JG13J148>
- Fyffe, C. L., Woodget, A. S., Kirkbride, M. P., Deline, P., Westoby, M. J., & Brock, B. W. (2020). Processes at the margins of supraglacial debris cover: Quantifying dirty ice ablation and debris redistribution. *Earth Surface Processes and Landforms*, 45(10), 2272–2290. <https://doi.org/10.1002/esp.4879>
- Garratt, J. R. (1992). *The atmospheric boundary layer*. Cambridge University Press.

- Garreaud, R. D., Boisier, J. P., Rondanelli, R., Montecinos, A., Sepúlveda, H. H., & Veloso-Aguila, D. (2020). The Central Chile Mega Drought (2010–2018): A climate dynamics perspective. *International Journal of Climatology*, *40*(1), 421–439. <https://doi.org/10.1002/joc.6219>
- Garreaud, R. D., Clem, K., & Veloso, J. V. (2021). The south pacific pressure trend dipole and the southern blob. *Journal of Climate*, *34*(18), 7661–7676. <https://doi.org/10.1175/JCLI-D-20-0886.1>
- Gibson, M. J., Glasser, N. F., Quincey, D. J., Mayer, C., Rowan, A. V., & Irvine-Fynn, T. D. (2017). Temporal variations in supraglacial debris distribution on Baltoro Glacier, Karakoram between 2001 and 2012. *Geomorphology*, *295*, 572–585. <https://doi.org/10.1016/j.geomorph.2017.08.012>
- Giese, A., Boone, A., Wagon, P., & Hawley, R. (2020). Incorporating moisture content in surface energy balance modeling of a debris-covered glacier. *The Cryosphere*, *14*(5), 1555–1577. <https://doi.org/10.5194/tc-14-1555-2020>
- Gruber, S., & Haeberli, W. (2007). Permafrost in steep bedrock slopes and its temperatures-related destabilization following climate change. *Journal of Geophysical Research*, *112*(2), 1–10. <https://doi.org/10.1029/2006JF000547>
- Herreid, S., & Pellicciotti, F. (2020). The state of rock debris covering Earth's glaciers. *Nature Geoscience*, *13*(9), 621–627. <https://doi.org/10.1038/s41561-020-0615-0>
- Humlum, O. (1997). Active layer thermal regime at three rock glaciers in Greenland. *Permafrost and Periglacial Processes*, *8*(4), 383–408. [https://doi.org/10.1002/\(sici\)1099-1530\(199710/12\)8:4<383::aid-ppp265>3.0.co;2-v](https://doi.org/10.1002/(sici)1099-1530(199710/12)8:4<383::aid-ppp265>3.0.co;2-v)
- Immerzeel, W. W., Petersen, L., Ragetli, S., & Pellicciotti, F. (2014). The importance of observed gradients of air temperature and precipitation for modeling runoff from a glacierized watershed in the Nepalese Himalayas. *Water Resources Research*, *50*(3), 2212–2226. <https://doi.org/10.1002/2013WR014506>
- IPG. (2022). Inventario Público de Glaciares. Dirección General de Aguas, Ministerio de Obras Públicas, Chile. Retrieved from <https://dga.mop.gob.cl/Paginas/InventarioGlaciares.aspx>
- Janke, J. R., Bellisario, A. C., & Ferrando, F. A. (2015). Classification of debris-covered glaciers and rock glaciers in the Andes of central Chile. *Geomorphology*, *241*, 98–121. <https://doi.org/10.1016/j.geomorph.2015.03.034>
- Juen, M., Mayer, C., Lambrecht, A., Wirbel, A., & Kueppers, U. (2013). Thermal properties of a supraglacial debris layer with respect to lithology and grain size. *Geografiska Annaler, Series A. Physical Geography*, *95*(3), 197–209. <https://doi.org/10.1111/geoa.12011>
- Laha, S., Winter-Billington, A., Banerjee, A., Shankar, R., Nainwal, H. C., & Koppes, M. (2022). Estimation of ice ablation on a debris-covered glacier from vertical debris-temperature profiles. *Journal of Glaciology*, *69*(273), 1–12. <https://doi.org/10.1017/jog.2022.35>
- Lettau, H. (1969). Note on aerodynamic roughness-parameter estimation on the basis of roughness-element description. *Journal of Applied Meteorology*, *8*(5), 828–832. [https://doi.org/10.1175/1520-0450\(1969\)008<0828:noarpe>2.0.co;2](https://doi.org/10.1175/1520-0450(1969)008<0828:noarpe>2.0.co;2)
- Mascart, P., Noilhan, J., & Giordani, H. (1995). A modified parameterization of flux-profile relationships in the surface layer using different roughness length values for heat and momentum. *Boundary-Layer Meteorology*, *72*(4), 331–344. <https://doi.org/10.1007/BF00708998>
- Mastrotheodoros, T., Pappas, C., Molnar, P., Burlando, P., Manoli, G., Parajka, J., et al. (2020). More green and less blue water in the Alps during warmer summers. *Nature Climate Change*, *10*(2), 155–161. <https://doi.org/10.1038/s41558-019-0676-5>
- McCarthy, M., Miles, E., Kneib, M., Buri, P., Fugger, S., & Pellicciotti, F. (2022). Supraglacial debris thickness and supply rate in High-Mountain Asia. *Communications Earth & Environment*, *3*(1), 269. <https://doi.org/10.1038/s43247-022-00588-2>
- McCarthy, M., Pritchard, H., Willis, I., & King, E. (2017). Ground-penetrating radar measurements of debris thickness on Lirung Glacier, Nepal. *Journal of Glaciology*, *63*(239), 543–555. <https://doi.org/10.1017/jog.2017.18>
- Melo Velasco, V., Miles, E., McCarthy, M., Shaw, T. E., Fyffe, C., Fontrodona-Bach, A., & Pellicciotti, F. (2024). Calculating debris properties with established methods at Pirámide Glacier, Chile [Dataset and Codes]. *Zenodo*. <https://doi.org/10.5281/zenodo.11581073>
- Miles, E. S., Steiner, J. F., & Brun, F. (2017). Highly variable aerodynamic roughness length (z_0) for a hummocky debris-covered glacier. *Journal of Geophysical Research: Atmospheres*, *122*(16), 8447–8466. <https://doi.org/10.1002/2017JD026510>
- Miles, E. S., Steiner, J. F., Buri, P., Immerzeel, W. W., & Pellicciotti, F. (2022). Controls on the relative melt rates of debris-covered glacier surfaces. *Environmental Research Letters*, *17*(6), 064004. <https://doi.org/10.1088/1748-9326/ac6966>
- Millan, R., Mouginot, J., Rabatel, A., & Morlighem, M. (2022). Ice velocity and thickness of the world's glaciers. *Nature Geoscience*, *15*(2), 124–129. <https://doi.org/10.1038/s41561-021-00885-z>
- Moore, P. L. (2018). Stability of supraglacial debris. *Earth Surface Processes and Landforms*, *43*(1), 285–297. <https://doi.org/10.1002/esp.4244>
- Moore, R. D. (1983). On the use of bulk aerodynamic formulae over melting snow. *Nordic Hydrology*, *14*(4), 193–206. <https://doi.org/10.2166/nh.1983.0016>
- Munro, D. S. (1989). Surface roughness and bulk heat transfer on a glacier: Comparison with eddy correlation. *Journal of Glaciology*, *35*(121), 343–348. <https://doi.org/10.1017/S0022143000009266>
- Nakawo, M., & Young, G. (1981). Field experiments to determine the effect of a debris layer on ablation of glacier ice. *Annals of Glaciology*, *2*, 85–91. <https://doi.org/10.3189/172756481794352432>
- Nakawo, M., & Young, G. J. (1982). Estimate of glacier ablation under a debris layer from surface temperature and meteorological variables. *Journal of Glaciology*, *28*(98), 29–34. <https://doi.org/10.1017/S002214300001176X>
- Nicholson, L., & Benn, D. I. (2006). Calculating ice melt beneath a debris layer using meteorological data. *Journal of Glaciology*, *52*(178), 463–470. <https://doi.org/10.3189/172756506781828584>
- Nicholson, L., & Benn, D. I. (2012). Properties of natural supraglacial debris in relation to modelling sub-debris ice ablation. *Earth Surface Processes and Landforms*, *38*(5), 490–501. <https://doi.org/10.1002/esp.3299>
- Nicholson, L., McCarthy, M., Pritchard, H. D., & Willis, I. (2018). Supraglacial debris thickness variability: Impact on ablation and relation to terrain properties. *The Cryosphere*, *12*(12), 3719–3734. <https://doi.org/10.5194/tc-12-3719-2018>
- Nicholson, L., & Stiperski, I. (2020). Comparison of turbulent structures and energy fluxes over exposed and debris-covered glacier ice. *Journal of Glaciology*, *66*(258), 543–555. <https://doi.org/10.1017/jog.2020.23>
- Nield, J. M., Chiverrell, R. C., Darby, S. E., Leyland, J., Vircavs, L. H., & Jacobs, B. (2013). Complex spatial feedbacks of tephra redistribution, ice melt and surface roughness modulate ablation on tephra covered glaciers. *Earth Surface Processes and Landforms*, *38*(1), 95–102. <https://doi.org/10.1002/esp.3352>
- Nield, J. M., King, J., Wiggs, G. F., Leyland, J., Bryant, R. G., Chiverrell, R. C., et al. (2013). Estimating aerodynamic roughness over complex surface terrain. *Journal of Geophysical Research: Atmospheres*, *118*(23), 948–961. <https://doi.org/10.1002/2013JD020632>
- Östrem, G. (1959). *Ice melting under a thin layer of Moraine, and the existence of ice cores in moraine ridges* (Vol. 41, 228–230). Swedish Society for Anthropology and Geography. Tech. Rep. No. 4. <https://doi.org/10.1080/20014422.1959.11907953>
- Petersen, E., Hock, R., Fochesatto, G. J., & Anderson, L. S. (2022). The significance of convection in supraglacial debris revealed through novel analysis of thermistor profiles. *Journal of Geophysical Research: Earth Surface*, *127*(9), 1–20. <https://doi.org/10.1029/2021JF006520>
- Quincey, D., Smith, M., Rounce, D., Ross, A., King, O., & Watson, C. (2017). Evaluating morphological estimates of the aerodynamic roughness of debris covered glacier ice. *Earth Surface Processes and Landforms*, *42*(15), 2541–2553. <https://doi.org/10.1002/esp.4198>

- Reid, T. D., & Brock, B. W. (2010). An energy-balance model for debris-covered glaciers including heat conduction through the debris layer. *Journal of Glaciology*, 56(199), 903–916. <https://doi.org/10.3189/002214310794457218>
- Reid, T. D., Carenzo, M., Pellicciotti, F., & Brock, B. W. (2012). Including debris cover effects in a distributed model of glacier ablation. *Journal of Geophysical Research*, 117(D18). <https://doi.org/10.1029/2012JD017795>
- Reyes Kutscher, G. B. (2023). *Evolución Geomorfológica Cuaternaria Tardía del Glaciar Cubierto Pirámide, Chile Central (33°S)*. [MSc Thesis]. Universidad de Chile. Retrieved from <https://repositorio.uchile.cl/handle/2250/198847>
- Rounce, D. R., Hock, R., McNabb, R. W., Millan, R., Sommer, C., Braun, M. H., et al. (2021). Distributed global debris thickness estimates reveal debris significantly impacts glacier mass balance. *Geophysical Research Letters*, 48(8). <https://doi.org/10.1029/2020GL091311>
- Rounce, D. R., King, O., McCarthy, M., Shean, D. E., & Salerno, F. (2018). Quantifying debris thickness of debris-covered glaciers in the Everest region of Nepal through inversion of a subdebris melt model. *Journal of Geophysical Research: Earth Surface*, 123(5), 1094–1115. <https://doi.org/10.1029/2017JF004395>
- Rounce, D. R., Quincey, D. J., & McKinney, D. C. (2015). Debris-covered glacier energy balance model for Imja–Lhotse Shar Glacier in the Everest region of Nepal. *The Cryosphere*, 9(6), 2295–2310. <https://doi.org/10.5194/tc-9-2295-2015>
- Rowan, A. V., Egholm, D. L., Quincey, D. J., & Glasser, N. F. (2015). Modelling the feedbacks between mass balance, ice flow and debris transport to predict the response to climate change of debris-covered glaciers in the Himalaya. *Earth and Planetary Science Letters*, 430, 427–438. <https://doi.org/10.1016/j.epsl.2015.09.004>
- Schaefer, M., Fonseca-Gallardo, D., Fariás-Barahona, D., & Casassa, G. (2020). Surface energy fluxes on Chilean glaciers: Measurements and models. *The Cryosphere*, 14(8), 2545–2565. <https://doi.org/10.5194/tc-14-2545-2020>
- Shao, Y., & Yang, Y. (2008). A theory for drag partition over rough surfaces. *Journal of Geophysical Research*, 113(2), 1–9. <https://doi.org/10.1029/2007JF000791>
- Shaw, T. E., Gascoin, S., Mendoza, P. A., Pellicciotti, F., & McPhee, J. (2020). Snow depth patterns in a high mountain Andean catchment from satellite optical tristereoscopic remote sensing. *Water Resources Research*, 56(2), 1–23. <https://doi.org/10.1029/2019WR024880>
- Shaw, T. E., Miles, E. S., Chen, D., Jouberton, A., Kneib, M., Fugger, S., et al. (2022). Multi-decadal monsoon characteristics and glacier response in High Mountain Asia. *Environmental Research Letters*, 17(10), 104001. <https://doi.org/10.1088/1748-9326/ac9008>
- Sicart, J. E., Litt, M., Helgason, W., Tahar, V. B., & Chaperon, T. (2014). A study of the atmospheric surface layer and roughness lengths on the high-altitude tropical Zongo glacier, Bolivia. *Journal of Geophysical Research: Atmospheres*, 119(7), 3793–3808. <https://doi.org/10.1002/2013JD020615>
- Smeets, C. J. P. P., & Broeke, M. R. (2008). The parameterisation of scalar transfer over rough ice. *Boundary-Layer Meteorology*, 128(3), 339–355. <https://doi.org/10.1007/s10546-008-9292-z>
- Steiner, J. F., Kraaijenbrink, P. D. A., & Immerzeel, W. W. (2021). Distributed melt on a Debris-Covered Glacier: Field observations and melt modeling on the Lirung Glacier in the Himalaya. *Frontiers in Earth Science*, 9(July), 1–21. <https://doi.org/10.3389/feart.2021.678375>
- Steiner, J. F., Litt, M., Stigter, E. E., Shea, J., Bierkens, M. F. P., & Immerzeel, W. W. (2018). The importance of turbulent fluxes in the surface energy balance of a Debris-Covered Glacier in the Himalayas. *Frontiers in Earth Science*, 6. <https://doi.org/10.3389/feart.2018.00144>
- Stull, R. B. (1988). In R. B. Stull (Ed.), *An introduction to boundary layer meteorology*. Dordrecht: Springer Netherlands. <https://doi.org/10.1007/978-94-009-3027-8>
- Swifthbank, C. (1950). The Origin of dirt cones on glaciers. *Journal of Glaciology*, 1(8), 461–465. <https://doi.org/10.3189/s0022143000012880>
- Waples, D. W., & Waples, J. S. (2004). A review and evaluation of specific heat capacities of rocks, minerals, and subsurface fluids. Part 2: Fluids and porous rocks. *Natural Resources Research*, 13(2), 123–130. <https://doi.org/10.1023/B:NARR.00000032648.15016.49>
- Westoby, M. J., Brasington, J., Glasser, N. F., Hambrey, M. J., & Reynolds, J. M. (2012). 'Structure-from-Motion' photogrammetry: A low-cost, effective tool for geoscience applications. *Geomorphology*, 179, 300–314. <https://doi.org/10.1016/j.geomorph.2012.08.021>
- Westoby, M. J., Rounce, D. R., Shaw, T. E., Fyffe, C. L., Moore, P. L., Stewart, R. L., & Brock, B. W. (2020). Geomorphological evolution of a debris-covered glacier surface. *Earth Surface Processes and Landforms*, 45(14), 3431–3448. <https://doi.org/10.1002/esp.4973>